

A mathematical model of action potentials of mouse sinoatrial node cells with molecular bases

Sanjay Kharche, Jian Yu, Ming Lei and Henggui Zhang

Am J Physiol Heart Circ Physiol 301:H945-H963, 2011. First published 1 July 2011;

doi: 10.1152/ajpheart.00143.2010

You might find this additional info useful...

This article cites 90 articles, 57 of which you can access for free at:
<http://ajpheart.physiology.org/content/301/3/H945.full#ref-list-1>

Updated information and services including high resolution figures, can be found at:
<http://ajpheart.physiology.org/content/301/3/H945.full>

Additional material and information about *American Journal of Physiology - Heart and Circulatory Physiology* can be found at:
<http://www.the-aps.org/publications/ajpheart>

This information is current as of August 29, 2012.

American Journal of Physiology - Heart and Circulatory Physiology publishes original investigations on the physiology of the heart, blood vessels, and lymphatics, including experimental and theoretical studies of cardiovascular function at all levels of organization ranging from the intact animal to the cellular, subcellular, and molecular levels. It is published 12 times a year (monthly) by the American Physiological Society, 9650 Rockville Pike, Bethesda MD 20814-3991. Copyright © 2011 the American Physiological Society. ISSN: 0363-6135, ESN: 1522-1539. Visit our website at <http://www.the-aps.org/>.

A mathematical model of action potentials of mouse sinoatrial node cells with molecular bases

Sanjay Kharche,¹ Jian Yu,¹ Ming Lei,^{2*} and Henggui Zhang^{1,3*}

¹Biological Physics Group, School of Physics and Astronomy; ²Cardiovascular Research Group, School of Biomedicine, University of Manchester, Manchester, United Kingdom; and ³School of Computer Science and Technology, Harbin Institute of Technology, Harbin, China

Submitted 10 February 2010; accepted in final form 28 June 2011

Kharche S, Yu J, Lei M, Zhang H. A mathematical model of action potentials of mouse sinoatrial node cells with molecular bases. *Am J Physiol Heart Circ Physiol* 301: H945–H963, 2011. First published July 1, 2011; doi:10.1152/ajpheart.00143.2010.—Genetically modified mice are popular experimental models for studying the molecular bases and mechanisms of cardiac arrhythmia. A postgenome challenge is to classify the functional roles of genes in cardiac function. To unveil the functional role of various genetic isoforms of ion channels in generating cardiac pacemaking action potentials (APs), a mathematical model for spontaneous APs of mouse sinoatrial node (SAN) cells was developed. The model takes into account the biophysical properties of membrane ionic currents and intracellular mechanisms contributing to spontaneous mouse SAN APs. The model was validated by its ability to reproduce the physiological exceptionally short APs and high pacing rates of mouse SAN cells. The functional roles of individual membrane currents were evaluated by blocking their coding channels. The roles of intracellular Ca^{2+} -handling mechanisms on cardiac pacemaking were also investigated in the model. The robustness of model pacemaking behavior was evaluated by means of one- and two-parameter analyses in wide parameter value ranges. This model provides a predictive tool for cellular level outcomes of electrophysiological experiments. It forms the basis for future model development and further studies into complex pacemaking mechanisms as more quantitative experimental data become available.

computer modeling; cardiac action potential; genetic isoforms; pacemaking mechanisms

THE CARDIAC EXCITATION SEQUENCE is initiated by the cardiac pacemaker, the sinoatrial node (SAN), and spreads throughout the heart. The function of the SAN is therefore understandably vital in cardiac physiology. The SAN produces spontaneous rhythmic action potentials (APs) via an emergent action of many interacting membrane ionic currents and intracellular processes (8). Experimental cell membrane ion channel patch-clamp data were first incorporated into a predictive mathematical model by Noble in 1962 (63), leading to the seminal “theory leading experiment.” It resulted in decades of extensive experimental discovery of a large number of cell membrane ion channels (2, 6, 15, 17, 18) and the study of pacemaking mechanisms in several mammalian species (9, 10, 20, 44, 81). These experimental data have been incorporated into increasingly complex mathematical models of SAN automaticity to simulate species-specific SAN AP waveforms (83) and have also been used to investigate the roles of ionic currents

and Ca^{2+} handling in cardiac pacemaking mechanisms (50, 78, 88, 90).

Despite these extensive electrophysiological studies, understanding of the underlying molecular basis of cardiac arrhythmogenesis remains limited. Pore-forming transmembrane proteins facilitating ionic currents are encoded by specific ion channel genes (54, 68). Tissue-specific expression of these ion channel genes and their functional impact on the tissue’s physiological (e.g., SAN pacemaking) and pathological (e.g., bradycardia) states are important issues to be addressed. In recent times, genetically modified mouse models have gained popularity in the study of clinical SAN dysfunction (39, 42). The mouse heart rate [~ 294 beats/min (10)], however, is much higher than that in larger mammals [rabbit: ~ 189 beats/min (14) to ~ 214 beats/min (74); human: ~ 73 beats/min (81)]. To fully appreciate such observations, the biophysical properties of ion channels and their genetic bases that regulate mouse SAN APs need further investigation.

A biophysically detailed mathematical model of mouse SAN APs will complement experimentation in underpinning the correlation between ion channel function and their genetic bases. However, most contemporary SAN models (13, 16, 36, 67, 89) do not consider isoform-specific channel gating and kinetics. A recent membrane delimited mouse SAN cell model (56) partially reproduced some experimental data of the mouse SAN but has fundamental limitations in simulating the functional roles of ion currents on mouse cardiac pacemaking (31). The present study aimed to further develop a biophysically detailed model of mouse SAN isolated cell APs with biophysically distinct ion channel isoforms and a detailed dynamic intracellular ionic mechanism.

GLOSSARY

α	Voltage-dependent opening rate constant
β	Voltage-dependent closing rate constant
τ	Time constant
4-AP	4-Aminopyridine
AP	Action potential
APA	AP amplitude
APD	AP duration
APD ₅₀	APD at 50% repolarization
APD ₉₀	APD at 90% repolarization
$[\text{Ca}^{2+}]_i$	Intracellular Ca^{2+} concentration or Ca^{2+} concentration in the cytosol
$[\text{Ca}^{2+}]_o$	Extracellular Ca^{2+} concentration
$[\text{Ca}^{2+}]_{\text{rel}}$	Ca^{2+} concentration in the JSR
$[\text{Ca}^{2+}]_{\text{sub}}$	Ca^{2+} concentration in the subspace
$[\text{Ca}^{2+}]_{\text{up}}$	Ca^{2+} concentration in the NSR

* M. Lei; and H. Zhang are joint senior authors.

Address for reprint requests and other correspondence: H. Zhang, School of Physics and Astronomy, Univ. of Manchester, Manchester M13 9PL, UK (e-mail: henggui.zhang@manchester.ac.uk).

CL	Cycle length	$I_{b,Na}$	Background Na^+ current
$[CQ]_{tot}$	Total calsequestrin concentration	I_{CaL}	L-type Ca^{2+} current
C_m	Cell membrane capacitance	$I_{CaL,1.2}$	L-type Ca^{2+} channel isoform $Ca_v1.2$ current
$[CM]_{tot}$	Total calmodulin concentration	$I_{CaL,1.3}$	L-type Ca^{2+} channel isoform $Ca_v1.3$ current
$d_{L,1.2}$	Activation gate for $I_{CaL,1.2}$	I_{CaT}	T-type Ca^{2+} current
$d_{L,1.3}$	Activation gate for $I_{CaL,1.3}$	$I_{CaT,3.1}$	T-type Ca^{2+} channel isoform $Ca_v3.1$ current
d_T	Inactivation gate of I_{CaT}	I_f	Hyperpolarization-activated current
dV/dt	Upstroke velocity of the AP	$I_{f,HCN4}$	HCN4 channel current
dV/dt_{max}	Maximum upstroke velocity of the AP	I_{fK}	K^+ component of I_f
DDR	Diastolic depolarization rate	I_{fNa}	Na^+ component of I_f
E_{Ca}	Reversal potential of Ca^{2+}	I_{K1}	Time-independent K^+ current
E_{CaL}	Reversal potential of $I_{CaL,1.2}$ and $I_{CaL,1.3}$	I_{Kr}	Rapid delayed rectifying K^+ current
E_{CaT}	Reversal potential of I_{CaT}	I_{Ks}	Slow delayed rectifying K^+ current
E_K	Reversal potential of K^+ currents	I_{Na}	Fast Na^+ current
E_{Ks}	Reversal potential of I_{Ks}	$I_{Na,1.1}$	Na^+ channel isoform $Na_v1.1$ current
E_{Na}	Reversal potential of Na^+ currents	$I_{Na,1.5}$	Na^+ channel isoform $Na_v1.5$ current
$E_{Na,1.5}$	Reversal potential of $I_{Na,1.5}$	I_{NaCa}	Na^+/Ca^{2+} exchanger current
E_{st}	Reversal potential of I_{st}	I_{NaK}	Na^+-K^+ pump current
EC _{50-SR}	EC ₅₀ for Ca^{2+} SR-dependent activation of SR Ca^{2+} release	I_{NaK}	Maximum I_{NaK}
f_{Ca}	Ca^{2+} -dependent inactivation gating variable for $I_{CaL,1.2}$ and $I_{CaL,1.3}$	I_{st}	Sustained inward Na^+ current
f_{CMi}	Fractional occupancy of calmodulin by $[Ca^{2+}]_i$	I_{sus}	Sustained component of 4-AP-sensitive currents
f_{CMs}	Fractional occupancy of calmodulin by $[Ca^{2+}]_{sub}$	I_{to}	Transient component of 4-AP-sensitive currents
f_{CQ}	Fractional occupancy of calsequestrin by $[Ca^{2+}]_{rel}$	I	Inactive fraction of RyR channels
$f_{L,1.2}$	Inactivation gate for $I_{CaL,1.2}$	Iso	Isoproterenol
$f_{L,1.3}$	Inactivation gate for $I_{CaL,1.3}$	$j_{1.1}$	Slow inactivation gating variable of $Na_v1.1$
f_T	Activation gate of I_{CaT}	$j_{1.5}$	Slow inactivation gating variable of $Na_v1.5$
f_{TC}	Fractional occupancy of the troponin Ca^{2+} site by $[Ca^{2+}]_i$	$j_{Ca,dif}$	Ca^{2+} diffusion flux from the subspace to the myoplasm
f_{TMC}	Fractional occupancy of the troponin Mg^{2+} site by $[Ca^{2+}]_i$	j_{rel}	Ca^{2+} release flux from the JSR to the subspace
f_{TMM}	Fractional occupancy of the troponin Mg^{2+} site by Mg^{2+}	j_{tr}	Ca^{2+} transfer flux from the NSR to the JSR
F	Faraday's constant	j_{up}	Ca^{2+} uptake flux from the myoplasm to the NSR
F_{Na}	Fraction of I_{Na} inactivating slowly	JSR	Junctional SR
g	Gating variable; conductance	k_{bCQ}	Ca^{2+} dissociation constant of calsequestrin
g_{∞}	Steady-state voltage-dependent value of gate g	k_{bCM}	Ca^{2+} dissociation constant of calmodulin
$g_{b,Na}$	Conductance of $I_{b,Na}$	k_{bTC}	Ca^{2+} dissociation constant of the troponin Ca^{2+} site
$g_{b,K}$	Conductance of $I_{b,K}$	k_{bTMC}	Ca^{2+} dissociation constant of the troponin Mg^{2+} site
$g_{b,Ca}$	Conductance of $I_{b,Ca}$	k_{bTMM}	Mg^{2+} dissociation constant of the troponin Mg^{2+} site
$g_{CaL,1.2}$	Conductance of $I_{CaL,1.2}$	k_{CaSR}	SR Ca^{2+} -dependent RyR activation coefficient
$g_{CaL,1.3}$	Conductance of $I_{CaL,1.3}$	k_{fCQ}	Ca^{2+} association constant of calsequestrin
g_{CaT}	Conductance of I_{CaT}	k_{fCM}	Ca^{2+} association constant of calmodulin
g_h	Conductance of I_f	k_{fTC}	Ca^{2+} association constant of troponin
g_{K1}	Conductance of I_{K1}	k_{fTMC}	Ca^{2+} association constant of the troponin Mg^{2+} site
g_{Kr}	Conductance of I_{Kr}	k_{fTMM}	Mg^{2+} association constant of the troponin Mg^{2+} site
g_{Ks}	Conductance of I_{Ks}	k_{iCa}	Baseline non-SR-dependent transition rate constant for the RyR
$g_{Na,1.1}$	Conductance of $I_{Na,1.1}$	k_{im}	Rate transition constant for RyR
$g_{Na,1.5}$	Conductance of $I_{Na,1.5}$	k_{iSRCa}	Ca^{2+} -dependent RyR rate constant not limited by diffusion
g_{st}	Conductance of I_{st}	k_{NaCa}	Scaling factor for I_{NaCa}
g_{sus}	Conductance of I_{sus}	k_{oCa}	Baseline non-SR-dependent transition rate constant for the RyR
g_{to}	Conductance of I_{to}	k_{om}	Rate transition constant for RyR
$h_{1.1}$	Fast inactivation gating variable of $Na_v1.1$	k_{oSRCa}	Ca^{2+} -dependent RyR rate constant not limited by diffusion
$h_{1.5}$	Fast inactivation gating variable of $Na_v1.5$	k_s	Release rate parameter
$hs_{1.1}$	Inactivating gating variable of $Na_v1.1$	K_{1ni}	Dissociation constant for $[Na^+]_i$ binding to the first site on the I_{NaCa} transporter
$hs_{1.5}$	Inactivating gating variable of $Na_v1.5$	K_{1no}	Dissociation constant for $[Na^+]_o$ binding to the first site on the I_{NaCa} transporter
HCN channels	Hyperpolarization-activated cyclic nucleotide-gated channels	K_{2ni}	Dissociation constant for $[Na^+]_i$ binding to the second site on the I_{NaCa} transporter
HSR	Parameter for Ca^{2+} -dependent activation of SR Ca^{2+} release	K_{2no}	Dissociation constant for $[Na^+]_o$ binding to second site on the I_{NaCa} transporter
I	Current		
$I_{b,Ca}$	Background Ca^{2+} current		
$I_{b,K}$	Background K^+ current		

K_{3ni}	Dissociation constant for $[Na^+]_i$ binding to the third site on the I_{NaCa} transporter
K_{3no}	Dissociation constant for $[Na^+]_o$ binding to the third site on the I_{NaCa} transporter
K_{ci}	Dissociation constant for $[Ca^{2+}]_{sub}$ binding to the I_{NaCa} transporter
K_{cni}	Dissociation constant for $[Na^+]_i$ and $[Ca^{2+}]_{sub}$ simultaneous binding to the I_{NaCa} transporter
K_{co}	Dissociation constant for $[Ca^{2+}]_o$ binding to the I_{NaCa} transporter
$K_{i,Ca}$	RyR Ca^{2+} -dependent inactivation rate
$K_{i,m}$	RyR repriming rate
K_{mf}	Forward-mode Ca^{2+} affinity of the SERCA pump
K_{mfCa}	Dissociation constant for Ca^{2+} -dependent inactivation of $I_{CaL,1.2}$ and $I_{CaL,1.3}$
$K_{m,K}$	Dissociation constant of K^+ activation of I_{NaK}
K_{mKp}	Half-maximal $[K^+]_o$ for I_{NaK}
$K_{m,Na}$	Dissociation constant of Na^+ activation of I_{NaK}
K_{mNap}	Half-maximal $[Na^+]_i$ for I_{NaK}
K_{mr}	Reverse-mode Ca^{2+} affinity of the SERCA pump
$K_{o,Ca}$	RyR Ca^{2+} activation rate
$K_{o,m}$	RyR deactivation rate
K_{rel}	Half-maximal $[Ca^{2+}]_{sub}$ of Ca^{2+} release from the JSR
K_s	Ca^{2+} release constant
K_{up}	Half-maximal $[Ca^{2+}]_i$ of Ca^{2+} uptake by j_{up} in the NSR
$[K^+]_i$	Intracellular K^+ concentration
$[K^+]_o$	Extracellular K^+ concentration
$m_{1.1}$	Activation gating variable of $Na_v1.1$
$m_{1.5}$	Activation gating variable of $Na_v1.5$
mERG1	Mouse <i>ether-a-go-go</i> -related gene 1
MaxSR	Ca^{2+} modeling parameter
MDP	Maximum diastolic potential
$[Mg^{2+}]_i$	Intracellular Mg^{2+} concentration
MaxSR	Ca^{2+} modeling parameter
MinSR	Ca^{2+} modeling parameter
n_{up}	SR Ca^{2+} uptake and Hill coefficient
$[Na^+]_i$	Intracellular Na^+ concentration
$[Na^+]_o$	Extracellular Na^+ concentration
NSR	Network SR
O	Open fraction of RyR channels
ODE	Ordinary differential equation
OS	Overshoot of the AP
p_a	Activation gating variable of I_{Kr}
p_i	Inactivation gating variable of I_{Kr}
P_{up}	Rate constant of Ca^{2+} uptake by j_{up} of the NSR
q	Inactivation gating variable of I_{to}
q_a	Activation gating variable of I_{st}
q_i	Inactivation gating variable of I_{st}
Q_{10}	Functional change in a variable with a 10-K increase in temperature
Q_{ci}	Fractional charge movement during the $[Ca^{2+}]_{sub}$ occlusion reaction of the I_{NaCa} transporter
Q_{co}	Fractional charge movement during the $[Ca^{2+}]_o$ occlusion reaction of the I_{NaCa} transporter
Q_n	Fractional charge movement during Na^+ occlusion reactions of the I_{NaCa} transporter
r	Activation gating variable of I_{to} and I_{sus}
R	Universal gas constant
R	Fraction of reactivated (closed) RyR channels
RI	Fraction of RyR inactivated channels
RyR	Ryanodine receptor

SAN	Sinoatrial node
SERCA	Sarco(endo)plasmic reticulum Ca^{2+} -ATPase
SR	Sarcoplasmic reticulum
t	Time
T	Absolute temperature (in K)
$[TC]_{tot}$	Total concentration of the troponin Ca^{2+} site
$[TMC]_{tot}$	Total concentration of the troponin Mg^{2+} site
TOP	Take off potential
V	Voltage
$V_{1/2}$	Voltage of half-activation or half-inactivation of ion channel gates
V_m	Membrane potential
V_{cell}	Cell volume
V_i	Myoplasmic volume available for Ca^{2+} diffusion
V_{rel}	Volume of the JSR
V_{sub}	Subspace volume
V_{up}	Volume of the NSR
x_s	Activation gating variable of I_{Ks}
y	Activation gating variable of I_f

MODEL DEVELOPMENT

The present model was primarily based on experimental data from isolated mouse SAN cells, from which biophysical parameters of Hodgkin-Huxley formulations of ionic currents were estimated. The model consists of 38 coupled ODEs describing voltage-gated ion channel currents, pump and exchanger currents, dynamic variations of intracellular ionic concentrations of Ca^{2+} ($[Ca^{2+}]_i$ and $[Ca^{2+}]_{sub}$), K^+ ($[K^+]_i$), and Na^+ ($[Na^+]_i$), and Ca^{2+} dynamics. A schematic diagram of the model is shown in Fig. 1. Model parameters for the basal cell model are shown in Table 1. The *Glossary* shows all abbreviations used in this report.

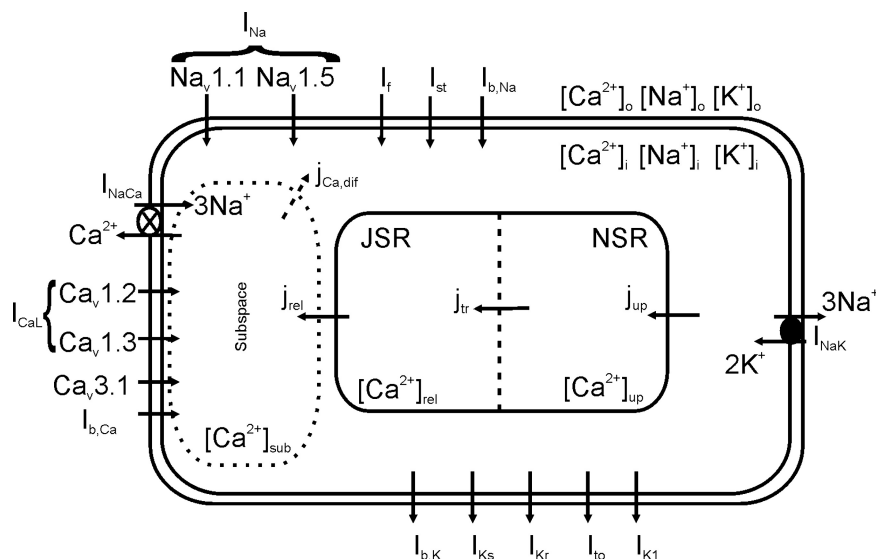
Cell Morphology

The cell volume of mouse pacemaking SAN myocytes ranges from 0.9 pl in spider-shaped cells to 5 pl in spindle-shaped cells (10, 39, 55). Our previous experimental recordings showed that cell C_m ranges from 20 to 60 pF (39). Therefore, a cell volume of 3 pl and a C_m of 25 pF were assumed in the present model for a primary SAN cell. The intracellular volumes relate to the cell volume in proportion to those in the Kurata et al. (36) model.

Descriptions of Membrane Currents and Ionic Homeostasis

The membrane currents considered in the mouse SAN cell model consist of I_{Na} ($I_{Na,1.1}$ and $I_{Na,1.5}$), I_{CaL} ($I_{CaL,1.2}$ and $I_{CaL,1.3}$), I_{CaT} , I_{st} , I_f ($I_{f,HCN4}$), I_{Kr} , I_{K1} , I_{NaCa} , I_{NaK} , and other miscellaneous currents (I_{Ks} , I_{sus} , I_{to} , and background currents). Wherever possible, biophysical parameters for these ionic currents were derived from experimental data of mouse SAN cells. Due to the limited availability of experimental data from the mouse SAN for some ionic channel currents, some parameters in the model were either based on parent models (36, 37, 89) or estimated to reproduce ion channel I - V relationships, experimentally observed mouse SAN AP features, and the functional role of individual modeling components. The formulations for cyclic oscillations of intracellular ionic concentrations and Ca^{2+} buffering in the cell compartments were adapted from Kurata et al. (36). To improve the effectiveness of SR function on modulating pacemaking APs, SERCA Ca^{2+} uptake and RyR Ca^{2+} release function mechanisms (i.e., Ca^{2+} pump-release mechanisms) were based on the formulation by Shannon et al. (73). A summary of the sources

Fig. 1. Schematic diagram of the mouse SAN cell models. The depolarizing (inward arrows) and repolarizing (outward arrows) cell membrane currents with isoformal detail along with the Ca^{2+} handling mechanism are shown. For abbreviations in this and all other figures, see the *Glossary*.



of experimental and modeling data is shown in Supplemental Material in Table S1.¹

I_{Na} ($I_{\text{Na},1.1}$ and $I_{\text{Na},1.5}$). The Na_v1.1 and Na_v1.5 isoforms predominantly compose mouse SAN I_{Na} (41). Na_v1.1 is uniform across the SAN. Na_v1.5 is spatially heterogeneous, with its channel current density increasing from the center toward the periphery (39). Both activate during the pacemaker potentials; Na_v1.1 activates at more positive potentials than Na_v1.5.

The models for the steady-state gating variables of I_{Na} were based on our experimental studies on isolated mouse SAN cells (Fig. S1, A and B) (39, 41). I_{Na} time kinetics in the present model were based on parent SAN models (36, 89). Maximum ionic current conductances for Na_v1.1 and Na_v1.5 isoforms were computed by comparing simulated I_{Na} I - V relationships to experimental data (Fig. S1C) (39, 41). Current traces of both isoforms during the voltage-clamp simulation are shown in Fig. S1D.

I_{CaL} ($I_{\text{CaL},1.2}$ and $I_{\text{CaL},1.3}$). The two isoforms contributing to I_{CaL} in the mouse SAN are the weakly expressed Ca_v1.2 isoform and the strongly expressed Ca_v1.3 isoform (52, 56).

In the model, the steady-state inactivation of Ca_v1.2 was based on experimental data (52), and the steady-state activation was adopted from a study by Mangoni et al. (56) (Fig. S2A). The steady states of activation and inactivation of Ca_v1.3 (Fig. S2B) were based on rabbit SAN experimental data as determined by Zhang et al. (89). Experimental data for mouse I_{CaL} time kinetics are as yet unavailable. It was found that SAN AP profiles depend strongly on I_{CaL} inactivation time kinetics at higher voltages (32). In the parent models, the inactivation time constant had a very large peak value (~ 310 ms at -40 mV) in the Kurata et al. (36) model and was kept almost constant at ~ 45 ms (over -40 mV) in the Zhang et al. (89) model. Since such a slow voltage-dependent inactivation of I_{CaL} produces a prolonged APD, the inactivation time kinetics of I_{CaL} of the Zhang et al. (89) model were adapted in this study. The reversal potentials for Ca_v1.2 and Ca_v1.3 were set to $+47$ mV based on experimental I - V data (10, 52).

The ionic current models were validated by simulating experimental I_{CaL} I - V relationships (52) for Ca_v1.2 and Ca_v1.3 isoforms (Fig. S2C). Current traces are shown in Fig. S2D. The maximum ionic current conductances so determined for both I_{CaL} isoforms (52) were found to give current densities significantly lower than in other reports [$I_{\text{CaL},1.2}$: 3.1 pA/pF at $+10$ mV (56) and $I_{\text{CaL},1.3}$: 10.4 pA/pF at -20

mV (56)]. The conductances were therefore augmented to give appropriate current densities during model pacemaking APs.

I_{CaT} . I_{CaT} is a voltage-dependent gated Ca^{2+} current with fast inactivation kinetics. I_{CaT} is expressed in the SAN of most species (22, 56) with a predominant isoform of Ca_v3.1 (7). In the mouse SAN, I_{CaT} has been shown to activate at approximately -65 mV, peak at approximately -30 mV, and have a reversal potential of $+45$ mV (10). The steady-state activation of I_{CaT} was adopted from previous modeling studies (36, 89). The steady-state gating properties are shown in Fig. S3A, which shows a small window current at -45 mV, close to the late phase of mouse SAN AP diastolic depolarization. The time kinetics of I_{CaT} were derived from experimental data (22) in previous models of I_{CaT} in the rabbit SAN. The ionic current model was validated by quantitatively comparing the simulated I_{CaT} I - V data with experimental data (10, 52, 56), as shown in Fig. S3B. The fast kinetics of I_{CaT} are evident from the current traces shown in Fig. S3C.

I_f . In the mouse SAN, the isoforms contributing to the native I_f are a heteromeric combination of HCN1, HCN2, and HCN4, with all being permeable to Na^+ and K^+ (3). It has been shown that the biophysical properties of individual isoforms coding I_f channels are different from each other (2), and their tandems (e.g., HCN1–HCN4 tandem) have distinct kinetics to native I_f . In the mouse SAN, it has been shown that HCN1 and HCN2 activate 25 times faster than HCN4 (61), and HCN4 is the predominant isoform compared with HCN1 and HCN2 (45). Therefore, a single native I_f was modeled in the present study. With experimental data showing a large range in the measured $V_{1/2}$ of I_f [-107 mV (10), -87.4 mV (55), -105 mV (26), -101 mV (1), and -106.8 mV (1)], a value of $V_{1/2} = -106.8$ mV was adopted in the present study (Fig. S4A). The slope of I_f activation was also based on experimental data (10, 66) and was taken to be -16.1 mV in the basal model. I_f time kinetics were based on experimental data of native I_f from mouse SAN cells (10), as shown in Fig. S4B. The model for I_f was validated by quantitatively comparing the simulated I_f I - V data with experimental data (10, 55, 66) (Fig. S4C). Simulated current traces for I_f are shown in Fig. S4D.

I_{st} . A novel SAN Na^+ current with I_{CaL} -like kinetics was first reported by Guo et al. (21) and has been observed in the SAN of several species (10, 21, 74). The voltage dependence of its gating kinetics are not available except for in the rat SAN. The gating kinetics of I_{st} were therefore based on experimental data obtained from the rat SAN (74). I_{st} in the mouse SAN activates around -80 mV and peaks at -60 mV (10). Both values are ~ 10 mV negative to those of the rat SAN. Therefore, a -10 -mV shift was implemented in

¹ Supplemental Material for this article is available at the *American Journal of Physiology-Heart and Circulatory Physiology* website.

Table 1. *Model parameter values in the basal cell model*

Model Parameters	Values
C_m , pF	25
$[Ca^{2+}]_o$, mM	1.8
$[CM]_{tot}$, mM	0.045
$[CQ]_{tot}$, mM	10
E_{CaL} , mV	47
E_{CaT} , mV	45
E_{st} , mV	17
$E_{Na,1.5}$, mV	41
F , C/M	96.485
$g_{b,Ca}$, nS/pF	0.0006
$g_{b,Na}$, nS/pF	0.00486
$g_{b,K}$, nS/pF	0.001
$g_{CaL,1.2}$, nS/pF	0.24
$g_{CaL,1.3}$, nS/pF	0.72
g_{CaT} , nS/pF	0.5586
g_h , nS/pF	0.228
g_{K1} , nS/pF	0.0324
g_{Kr} , nS/pF	0.09456
g_{Ks} , nS/pF	0.01196
$g_{Na,1.5}$, nS/pF	2.37×10^{-4}
$g_{Na,1.1}$, nS/pF	2.37×10^{-4}
g_{st} , nS/pF	0.0024
g_{sus} , nS/pF	0.0156
g_{to} , nS/pF	0.1968
I_{NaK} , pA/pF	5.698
k_{bCM} , ms^{-1}	0.542
k_{bCQ} , ms^{-1}	0.445
k_{bTC} , ms^{-1}	0.446
k_{bTCM} , ms^{-1}	0.00751
k_{bTMM} , ms^{-1}	0.751
k_{fCM} , mM^{-1}/ms	237.7
k_{fCQ} , mM^{-1}/ms	0.534
k_{fTC} , mM/ms	88.8
k_{fTCM} , mM/ms	237.7
k_{fTMM} , mM/ms	2.277
K_{mfCa} , mM	0.00035
$K_{m,K}$, mM	1.4
$K_{m,Na}$, mM	14
K_{NaCa} , pA/pF	220
K_{1ni} , mM	395.3
K_{1no} , mM	1628
K_{2ni} , mM	2.289
K_{2no} , mM	561.4
K_{3ni} , mM	26.44
K_{3no} , mM	4.663
K_{ci} , mM	0.0207
K_{co} , mM	3.663
K_{cni} , mM	26.44
Q_{ci}	0.1369
Q_{co}	0
Q_n	0.4315
$[K^+]_o$, mM	5.4
K_{up} , mM	0.0006
$[Mg^{2+}]_i$, mM	2.5
$[Na^+]_o$, mM	140
P_{up} , mM/ms	0.04
n_{up}	2
K_{mf} , mM	0.000246
K_{mr} , mM	3.29
R , $J \cdot mol^{-1} \cdot K^{-1}$	8.314
T , K	310.5
$[TC]_{tot}$, mM	0.031
$[TMC]_{tot}$, mM	0.062
V_{cell} , pL	3
V_i , pL	1.346
V_{rel} , pL	0.0036

*Continued*Table 1.—*Continued*

Model Parameters	Values
V_{sub} , pL	0.03328
V_{up} , pL	0.0348
α_{fCa}	0.021
$\tau_{Ca,dif}$, ms	0.04
τ_{tr} , ms	40
EC_{50_SR}	0.45
K_{oCa} , Mm^{-2}	10
K_{om} , ms^{-1}	0.06
K_{iCa} , $mM^{-1} ms^{-1}$	0.5
K_{im} , ms^{-1}	0.005
K_{ss} , ms^{-1}	130×10^4
HSR	2.5
MaxSR	15
MinSR	1

For model parameter definitions, see the *Glossary*.

the steady-state gating kinetics to fit experimental mouse SAN $I-V$ data. Mouse SAN I_{st} has a reversal potential of around +17 mV. The I_{st} model reproduced experimental $I-V$ data (10) (Fig. S4E) and current traces (Fig. S4F).

I_{Kr} . The primary protein regulating mouse SAN I_{Kr} is mERG1 (11). The model for I_{Kr} steady-state activation was based on experimental data (10, 58), whereas the steady state of inactivation was adapted from a previous study (36) (Fig. S5A). The activation time kinetics were based on experimental data (11). Since the experimental data were acquired at 28°C, a Q_{10} temperature correction of 1.4 (11, 60) was applied (Fig. S5B). I_{Kr} inactivation kinetics were adapted from a previous rabbit model (36). The I_{Kr} model was validated by simulating experimental $I-V$ data (Fig. S5C) and current traces (Fig. S5D) (10, 55).

I_{K1} . Maximum ionic current conductance of the mouse SAN I_{K1} model was based on experimental data of Cho et al. (10) obtained from mouse SAN cells and included a dependence on $[K^+]_o$.

Miscellaneous membrane currents. The other currents that the model consists of are I_{Ks} , 4-AP-sensitive I_{sus} and I_{to} , I_{NaCa} , I_{NaK} , and I_b , each of which were either based on experimental data or inherited from parent models. For example, the steady-state activation and kinetics of I_{Ks} were based on experimental data obtained from guinea pig SAN cells (24, 58). Equations for I_{sus} and I_{to} were based on parent rabbit SAN cell models (36, 89). The model for I_{NaCa} was adopted from Kurata et al. (36) and simulated the saturation characteristics of I_{NaCa} at large values of $[Ca^{2+}]_{sub}$. The scaling parameter k_{NaCa} was set to 220 pA/pF in the basal model to simulate physiological oscillations of $[Ca^{2+}]_i$ and $[Ca^{2+}]_{sub}$ (Fig. S6) and to facilitate a strong coupling between the intracellular and membrane pacemaking mechanisms.

Ionic Homeostasis in Mouse SAN Cells

Na⁺ and K⁺ concentrations. The simultaneous direct measurement of APs and intracellular ion concentrations is a formidable task experimentally (59), providing limited data to facilitate a quantitative description of the dynamic intracellular variations of $[Na^+]_i$ and $[K^+]_i$ (see for, e.g., Refs. 16 and 28) in a mathematical model of cardiac cells. The present basal model incorporated the dynamics of $[Na^+]_i$ and $[K^+]_i$ based on an ionic material balance. I_{NaK} was optimized to simulate stable oscillations of the intracellular ion concentrations.

Ca²⁺ homeostasis, buffers, and SR function. There is growing experimental evidence of the role of intracellular Ca^{2+} in modulating pacemaking APs of the mouse SAN (57, 62) via I_{NaCa} , which contributes to the diastolic depolarization phase of the AP (9, 84). Intracellular Ca^{2+} has also been shown to play an important role in the late diastolic depolarization phase of cat pacemaking APs (29, 44) via I_{CaT} . Depletion of Ca^{2+} by challenging RyR function (i.e., reduced Ca^{2+} release from the SR) has been shown to reduce pacemaking in

isolated mouse SAN cells (62). Mathematical modeling has also shown that a strong interaction between intracellular Ca^{2+} and membrane ionic processes regulates pacemaking APs (6, 50). In the present model, we started by incorporating the Ca^{2+} buffering formulations of Kurata et al. (36). Second, the SERCA Ca^{2+} uptake mechanism was based on the formulation by Shannon et al. (73), which models Ca^{2+} uptake from the cytosol to the NSR. The values of parameters for the SERCA pump vary widely among various modeling studies (69–71, 73). In this study, the Hill coefficient was set to 2 and the affinity of the forward mode of the pump to $0.246 \mu\text{M}$ to reflect measurements in rodents (69). The other parameters were optimized to maintain an $\sim 0.1 \mu\text{M}$ peak free $[\text{Ca}^{2+}]_i$ in the cytosol (36). Finally, the Ca^{2+} release mechanism to simulate RyR function was also based on the formulation of the Shannon et al. (73) multistate RyR “ Ca^{2+} clock” model. The RyR Ca^{2+} release model was optimized by Maltsev and Lakatta (50) for rabbit SAN cell pacemaking APs with longer a CL of ~ 315 ms. Since the CL of mouse SAN cell APs is much shorter (~ 200 ms) and is regulated by several ionic channel currents with much larger densities, we therefore further modified the parameters of the Shannon et al. (73) model for modeling the Ca^{2+} clock in our mouse SAN cell model.

Numerical Integration and Stability of Solutions

Integration method. The presented mouse SAN cell model consists of a 38 variable coupled stiff nonlinear ODE system. A standard explicit Euler integration method with a constant time step ($dt = 10^{-3}$ ms) was found to give stable solutions. Further reduction of the time step or implementation of a fourth-order Runge-Kutta integration method gave the same simulation results within 0.1% tolerance levels while increasing the computational time and effort. Simulations were carried out on a Sun Sparc with Solaris 9 using C programming.

Free parameters values, stability of solution, and determination of initial conditions. Biophysically detailed cardiac models consist of a large numbers of variables (~ 10 – 100) and parameters (in excess of 100) (32). The basal model was primarily based on experimental data associating the majority of the modeling parameters to experimentally observed electrophysiological data. Biophysical parameters not available in experimental data were taken from the parent models (36, 37, 89) and adapted to give typical AP characteristics in mouse SAN cells. For details of all inherited features, see Table S1.

For the determination of stable intracellular ionic oscillations, mass balance based on the ionic conservation principle was applied (33, 77). During the time integration, the accumulation or depletion of all intracellular ions was monitored. Oscillations of all intracellular ionic concentrations were stabilized within a tolerance of 1% variation. For example, the concentrations of $[\text{Na}^+]_i$ and $[\text{K}^+]_i$ were stabilized around average physiological values of 8 and 140 mM, respectively, by minimally adjusting the maximum I_{NaK} . It should be emphasized that the free parameters were estimated by minimal modifications to basal values. Consideration of dynamic variations in $[\text{Na}^+]_i$ and $[\text{K}^+]_i$ did not give rise to increased degeneracy and drift in the presented models (35), as seen predominantly in atrial and ventricular models (28, 46). This is due to the mass balance-based parametric fine tuning and the spontaneously beating SAN APs not requiring an extracellular stimulus. Such parametric fine tuning will nonetheless allow some drift and has been minimized in this study, as described above. The degeneracy and drift could be limited by maintaining constant $[\text{Na}^+]_i$ and $[\text{K}^+]_i$. This would, however, have rendered the function of I_{NaK} to be basically a background current. It should be noted that model development is, essentially, an iterative process, with novel experimental data being incorporated into the models continually.

Once the free parameters were determined, the initial conditions and stability of the solutions were estimated. To determine the

Table 2. Initial conditions for the basal cell model

Model Variables	Initial Values
V , mV	−64.6508005232
q_a	0.6185734202
q_i	0.4571815638
d_T	0.0015910627
f_T	0.4307958088
p_a	0.4033900505
p_i	0.9254742549
x_s	0.0127072059
$f_{L,1,2}$	0.9969251824
$d_{L,1,2}$	0.0000044417
$f_{L,1,3}$	0.9812943664
$d_{L,1,3}$	0.0001993197
f_{Ca}	0.7679518810
r	0.0045587632
q	0.6140737444
$m_{1,5}$	0.3991763968
$h_{1,5}$	0.2765325493
$j_{1,5}$	0.0252682289
$m_{1,1}$	0.1069853058
$h_{1,1}$	0.4548050890
$j_{1,1}$	0.0272302605
y	0.0281231662
$[\text{Ca}^{2+}]_i$, mM	0.0000326892
$[\text{Ca}^{2+}]_{rel}$, mM	0.1038669181
$[\text{Ca}^{2+}]_{up}$, mM	0.1038669181
$[\text{Ca}^{2+}]_{sub}$, mM	0.0000534741
f_{TC}	0.0000534741
f_{TMC}	0.1771999779
f_{TMM}	0.7268211576
f_{CMs}	0.0231294040
f_{CMi}	0.0142601584
f_{CQ}	0.1067137942
$[\text{Na}^+]_i$, mM	8.10311
$[\text{K}^+]_i$, mM	139.9221122
R	0.7717873638
O	0.0000000737
I	0.0000000207
RI	0.2173099253

For model variable definitions, see the Glossary.

initial conditions, all 38 variables were set to values expected at MDP. Thus, the value of V_m was set to -65 mV. Initial values of 0 and 1 were assigned to the activation and inactivation gates, respectively. All ionic concentrations were set at anticipated physiological diastolic levels (e.g., $[\text{Ca}^{2+}]_i = 0.1 \mu\text{M}$, $[\text{Na}^+]_i \sim 8$ mM, and $[\text{K}^+]_i \sim 140$ mM). The initial conditions for the RyR model four variables (O , I , R , and RI) were set to suitable nonzero values. The dynamic spontaneously oscillating model was then integrated for 1,000 s. In the final 100 s of simulated activity, the beat-to-beat variation of all the 38 variables was monitored. When the variation was below tolerance values, the solution was deemed to be stable. Values of all variables at MDP were then noted as initial conditions, as shown in Table 2.

Typically found in gating kinetics and in ion current formulations, which are all functions of V_m , division by small numbers close to machine precision makes the models unsuitable for numerical analysis. All above integrations were carried out by eliminating singularities in the modeling logical expressions (46) by performing a first-order Taylor expansion around all the relevant singularity values, and the approximations held valid with a range of 0.05 mV around the singularity.

RESULTS

Figure 2A shows the simulated time course of mouse SAN APs together with dynamic variation of the major ion

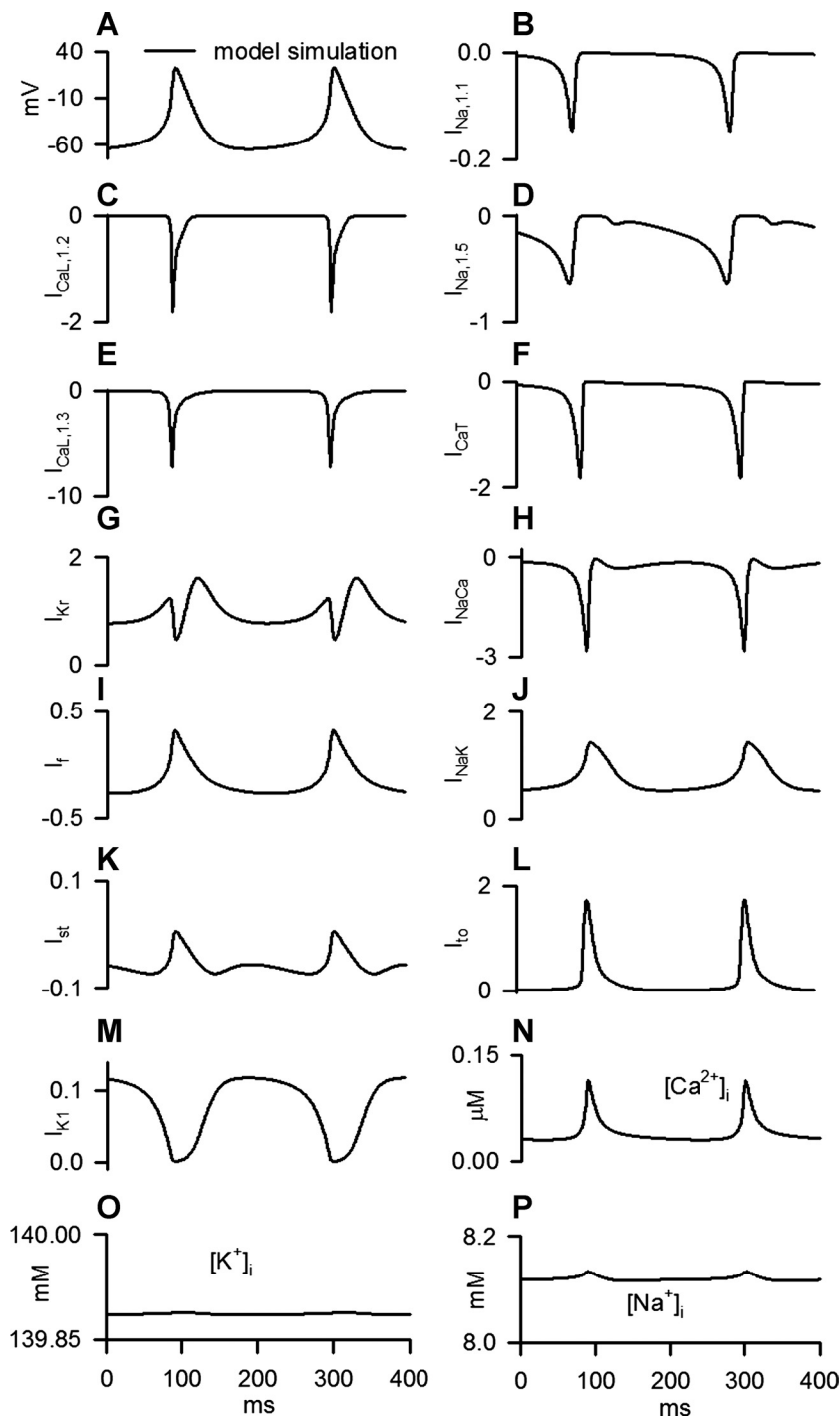


Fig. 2. Model-generated APs, ionic currents, and $[Ca^{2+}]_i$ transients in the basal model. A: model-generated APs. B–M: ionic currents during APs, normalized to C_m (in units of pA/pF). N: simulated $[Ca^{2+}]_i$ transients. O: dynamic $[K^+]_i$ variation during the AP. P: dynamic $[Na^+]_i$ variation during the AP.

channel currents and intracellular ion concentrations. The simulated APs have a rapid depolarizing upstroke, short APD, and fast pacemaking rate, which agree with the unique features of isolated mouse SAN cell APs. Figure S6 shows details of the dynamic variations of intracellular Ca^{2+} variables. It can be seen that the model produces $[Ca^{2+}]_i$ oscillations with an amplitude of 0.1 μM , which is close to experimental data (36). $[Ca^{2+}]_{sub}$ oscillations have systolic and diastolic values of 1,744 and 69.6 nM, respectively, which are comparable with experimental observations in rabbit SAN cells (51). To validate the model, simulated APs

and ion channel blocking simulations were compared with experimental data as detailed below.

Simulated APs and Experimental Recordings

Simulated APs were validated against experimental recordings, as shown in Fig. 3. Simulated AP characteristics, i.e., CL, APD₅₀, APD₉₀, OS, MDP, dV/dt_{max} , TOP, and DDR, agreed well with the experimental data, which further validated the use of parameters in the equations of individual ionic currents. Quantitative results are shown in Table 3 along with quantita-

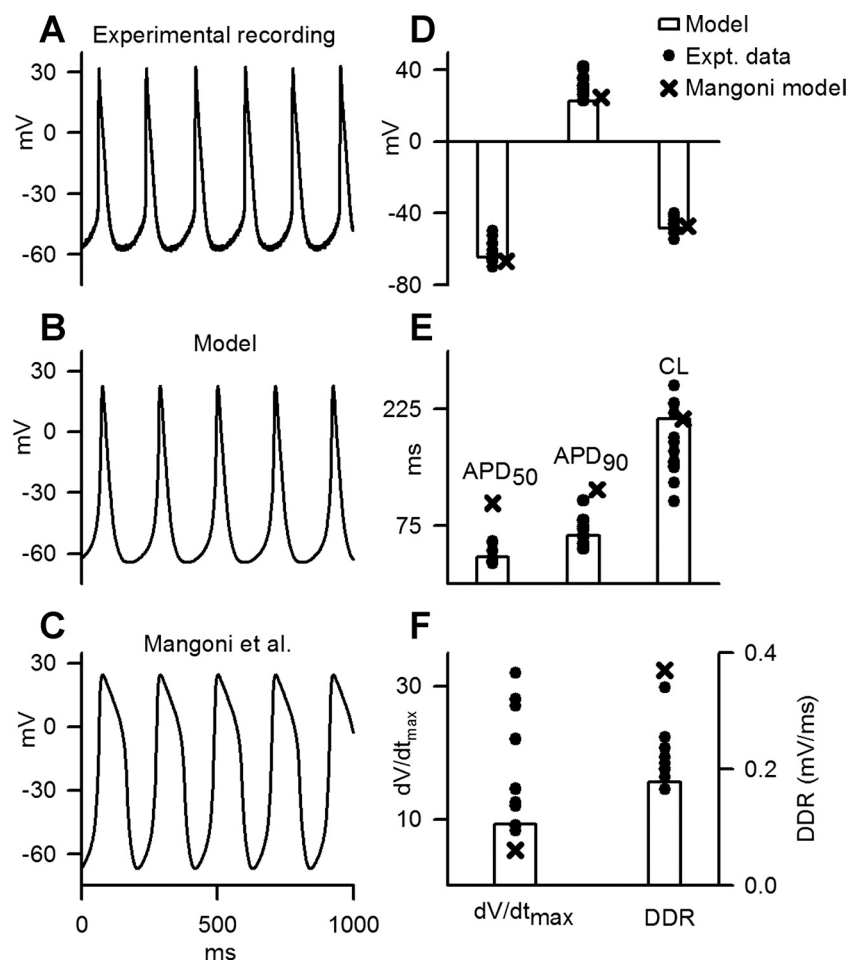


Fig. 3. Mouse SAN APs and characteristics. *A*: experimental AP recording from mouse SAN cells (solid line) ($C_m \sim 26$ pF) from our laboratory. *B*: simulated SAN AP in the basal model. *C*: simulated AP from Mangoni et al. (56) mouse SAN model. *D*: simulated MDP, OS, and TOP (open bars), experimental data (●), and Mangoni et al. (56) model data (×). The same nomenclature for modeling and experimental data apply to *E* and *F*. *E*: simulated APD₅₀, APD₉₀, and CL, experimental data, and Mangoni et al. (56) model data. *F*: simulated dV/dt_{max} and DDR along with experimental data and Mangoni et al. (56) model data. Data in *D–F* were obtained from quantitative results or from analysis of single cell AP profiles by Cho et al. (10), Lei et al. (39, 41), Mangoni et al. (52, 55), Clark et al. (11), Zhang et al. (91), Verheijck et al. (80), Alig et al. (1), Wu et al. (84), and Chen et al. (9).

tive experimental AP characteristics and Mangoni et al. (56) model simulation.

Roles of Individual Ionic Channel Currents in the Genesis of Mouse SAN APs

The functional roles of ion channels were investigated by isoform-specific ion channel blocking simulations and comparison with experimental data.

Role of I_{Na} . Simulation of block of $I_{Na,1.1}$ and $I_{Na,1.5}$ in the model is shown in Fig. 4. As shown in Fig. 4A, block of $I_{Na,1.1}$ did not affect the model pacemaking (CL increased from 212.12 to 217.01 ms), but block of $I_{Na,1.5}$ augmented CL by 32.5% (CL = 281.14 ms). Block of both isoforms simultaneously augmented CL by 38.2% (CL = 293.27 ms). The simulations are in agreement with our experimental results (41), where a 27% increase of CL was observed due to

inhibition of I_{Na} using 30 μ M TTX. A similar functional role of I_{Na} in the rabbit SAN has been observed by Kurata et al. (37). Although I_{Na} is not the main upstroke current in SAN cells and does not affect dV/dt_{max} (Fig. 4A, bottom), it contributes to pacemaking since both isoforms are active in the late diastolic depolarization pacemaker potential range (Fig. S1, A and B). This was reflected in the reduced DDR when I_{Na} was blocked in our basal model (Fig. 4B). Since I_{Na} acts predominantly in the late diastolic depolarization phase, block of I_{Na} did not affect APD and marginally reduced dV/dt_{max} in the model. Experimentally, however, we have observed that low (100 nM) or high (30 μ M) concentrations of TTX used to block $I_{Na,1.1}$ or $I_{Na,1.5}$, respectively, caused a reduction of dV/dt_{max} . This may be due to TTX affecting other depolarizing Ca^{2+} currents in SAN cells, as has been seen in experimental studies (75, 87).

Table 3. Experimental data and simulated mouse SAN AP characteristics from Mangoni et al. (56) and our basal models

	CL, ms	APD ₅₀ , ms	APD ₉₀ , ms	OS, mV	MDP, mV	dV/dt_{max} , V/s	TOP, mV	DDR, V/s
Experimental data range	106.1 to 255	26.3 to 56.88	45.8 to 107.14	22.7 to 42.0	-70 to -52	8.2 to 32	-54.6 to -40	0.172 to 0.34
Mangoni et al. model	212.31	104.00	121.1	24.6	-66.87	5.31	-47.3	0.3701
Present cell model	212.21	35.04	62.00	22.60	-64.52	9.20	-48.45	0.1786

Experimental data were obtained from quantitative results or from analysis of single cell AP profiles by Cho et al. (10), Lei et al. (39, 41), Mangoni et al. (52, 55), Clark et al. (11), Zhang et al. (91), Verheijck et al. (80), Alig et al. (1), Wu et al. (84), and Chen et al. (9). For definitions of the AP characteristics, see the *Glossary*.

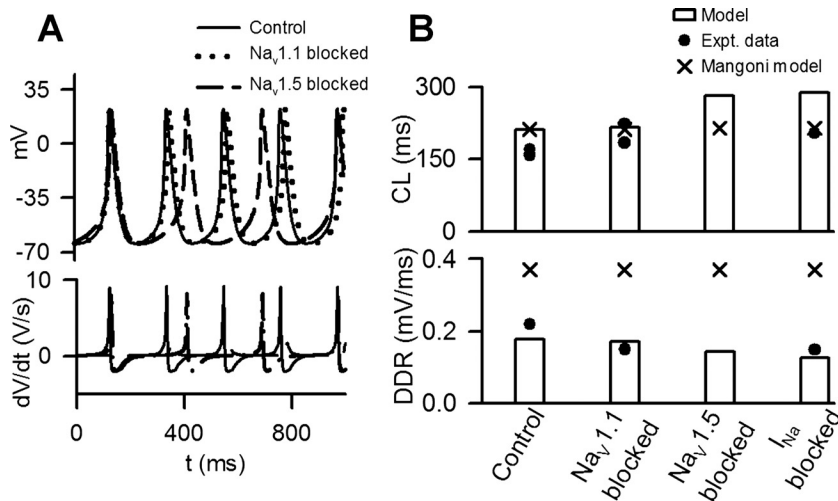


Fig. 4. Functional role of I_{Na} in the mouse SAN cell model. *A*, top: AP profiles under control (solid line), $Na_v1.1$ blocked (dashed line, almost coincidental with the control), and $Na_v1.5$ blocked (dashed-dotted line) conditions. *Bottom*, dV/dt during APs. *B*: CL (top) and DDR (bottom) under control and $Na_v1.1$, $Na_v1.5$, and I_{Na} blocked conditions. Shown are the model simulation (open bars), experimental data (●) (41), and Mangoni et al. (56) model simulation data (×).

To further investigate the functional role of $I_{Na,1.5}$ in mouse SAN pacemaking, the effects of alterations of $g_{Na,1.1}$ and $g_{Na,1.5}$ were simulated in the model (Fig. S7). Reduction of either isoform-specific conductance slowed down pacemaking, whereas increased conductance caused the expected progressive acceleration of pacemaking.

Role of I_{CaL} . Block of $I_{CaL,1.2}$ in the model (Fig. 5A) marginally increased CL by 0.2%, which was accompanied by reduced dV/dt_{max} , APA, and APD. Our simulations were similar to experimental data from rabbit SAN cells (34), where block of I_{CaL} by nifedipine in small balls from central SAN tissue accelerated pacemaking, reduced dV/dt_{max} , and reduced APA. Since the activation potential of $I_{CaL,1.2}$ is higher than TOP, its functional role in pacemaking activity is primarily in the modulation of OS, rather than the pacemaking rates (Fig.

S8). The limited role of $I_{CaL,1.2}$ on APs is due to its relatively small window current and small current density compared with $I_{CaL,1.3}$ (Fig. S2). The Mangoni et al. (56) model showed a small reduction of pacemaking rates upon inhibition of $I_{CaL,1.2}$.

The functional role of $Ca_v1.3$ on mouse SAN pacemaker activity was studied by blocking $I_{CaL,1.3}$ (Fig. 5B). Experimentally, $Ca_v1.3^{-/-}$ mice showed significantly slower pacemaking with prolonged CL or even an arrest in pacemaking activity (52). Such a negative chronotropic effect due to reduced $I_{CaL,1.3}$ on heart rates has also been observed in vivo, where $Ca_v1.3$ knockout mice showed prolonged PR intervals with a high incidence of sinus bradycardia (91). In the present model, block of $I_{CaL,1.3}$ by 45% produced a 17.33% increase in CL. Complete block abolished autorhythmic APs, leading to a stable resting potential of -40.47 mV. The Mangoni et al. (56)

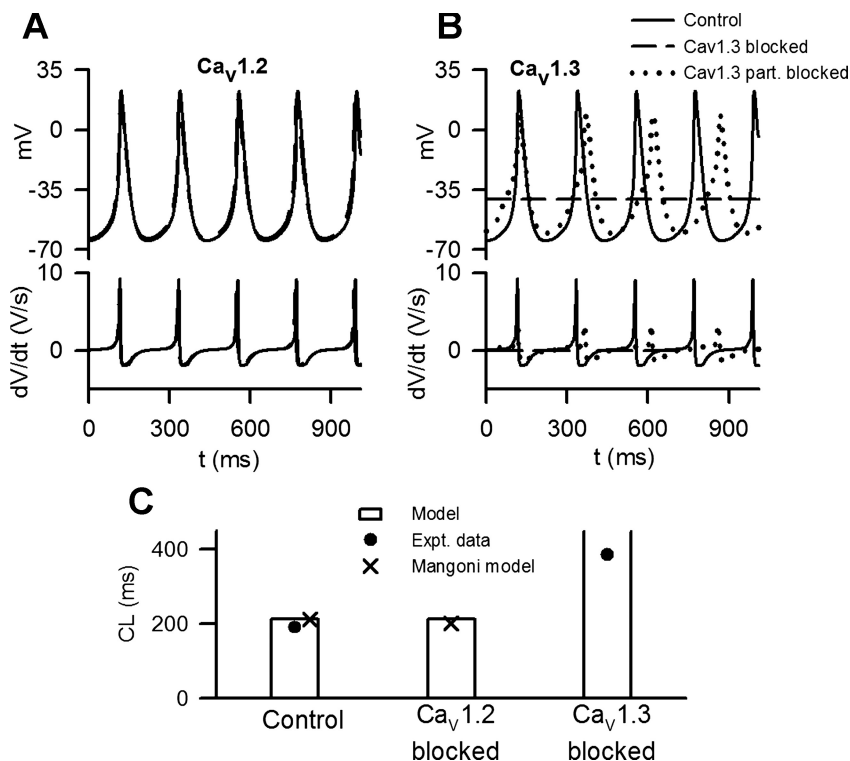


Fig. 5. Functional effects of block of I_{CaL} isoforms. *A*, top: AP profiles under control (solid line) and $Ca_v1.2$ blocked (dashed line) conditions. *Bottom*, dV/dt . *B*, top: AP profiles under control (solid line), partial block of $Ca_v1.3$ by 45% (dotted line), and total $Ca_v1.3$ blocked (dashed line) conditions. *Bottom*, dV/dt during APs. *C*: CL under control, $Ca_v1.2$ blocked, and $Ca_v1.3$ blocked conditions. Shown are the model simulation (open bars), experimental data (●), and Mangoni et al. (56) model simulation data (×).

model also showed a similar arrest of pacemaking upon $I_{CaL,1.3}$ block (stable resting potential at -29.3 mV). When both $I_{CaL,1.2}$ and $I_{CaL,1.3}$ were blocked in the model, pacemaking in the model was arrested with a stable resting potential of -40.8 mV. Changes in CL are shown in Fig. 5C.

The effects of altered $g_{CaL,1.3}$ on pacemaking were simulated in the model. $I_{CaL,1.3}$ is a vital regulator of OS and APD, as shown in Fig. S8. A decrease in $I_{CaL,1.3}$ slowed down pacemaking APs, resulting in increased CL along with dramatically reduced APAs. Augmenting $I_{CaL,1.3}$ accelerated pacemaking APs, resulting in reduced CL along with increased APAs and dV/dt_{max} .

Role of I_{CaT} . Experiments using $Ca_v3.1$ knockout mice have shown a pacemaking rate reduction by 34% (56). Studies in cat atria by Huser et al. (29) and Zhou and Lipsius (92) have also shown that a Ni^{2+} -induced reduction of I_{CaT} causes a 35–230% prolongation of CL, indicating the critical importance of I_{CaT} in SAN pacemaking. In the model, complete I_{CaT} block dramatically slowed down the pacemaking, with CL increasing by 49.1% (Fig. 6A). As observed experimentally (29), I_{CaT} block revealed that the reduction of CL was directly related to the reduced level of diastolic Ca^{2+} (Fig. 6B). In model simulations, I_{CaT} block produced a 38% reduction of peak $[Ca^{2+}]_i$ and a 42.79% reduction of $[Ca^{2+}]_{sub}$ as well as reduced Ca^{2+} release during DDR. The simulated changes of $[Ca]_i$ and $[Ca]_{sub}$ in response to I_{CaT} block were greater than the experimental data of Huser et al. (29), who observed an initial reduction of the $[Ca^{2+}]_{sub}$ pedestal during the diastolic depolarization phase but no remarkable change in peak $[Ca^{2+}]_{sub}$ or $[Ca^{2+}]_i$. This is possibly due to the fact that in the model, I_{CaT} is a major contributor to DDR and it plays an important role (secondary to I_{CaL}) in the early upstroke. Such a discrepancy

between the model simulation and experimental data suggest a possible limitation of the model, which requires further improvements when more experimental data on the biophysical properties of mouse I_{CaT} become available. As I_{CaT} activates during the DDR phase, the increase in CL arising from I_{CaT} block is primarily due to a decrease in DDR (see Fig. S9). Our simulation results are quantitatively similar to the experimentally observed role of I_{CaT} . I_{CaT} block produced a 6.2% increase of CL in the Mangoni et al. (56) model. Previous models of rabbit SAN cells have assumed a small maximal conductance of I_{CaT} , limiting its role in pacemaking dynamics. However, I_{CaT} has been experimentally observed to play a significant role in mouse SAN pacemaking and an even greater role in cat SAN cell pacemaking, as observed by Huser et al. (29). In the present model, the important role of I_{CaT} is reflected in its effects on CL and DDR (Fig. S9, A and B). Furthermore, the role of I_{CaT} was investigated in a two-parameter analysis, where g_h and P_{up} (parameters regulating the diastolic depolarization, along with g_{CaT}) were simultaneously varied in the presence and absence of I_{CaT} . As shown in Fig. S9C, the absence of I_{CaT} augmented the CL of stable pacemaking APs dramatically and reduced model robustness. Furthermore, the absence of I_{CaT} caused pacemaking arrest or aperiodic firing in a larger parametric range. The parameter analysis revealed the critical role of I_{CaT} in assuring the robustness of mouse SAN pacemaking activities.

Role of I_{st} . I_{st} has been observed in pacemaking SAN cells of several species (10, 20, 21). I_{st} has been observed in the mouse (10) and was incorporated as a small maximum conductance current in the model. A larger conductance of I_{st} caused the model to become unstable. Block of I_{st} in the model (Fig. 7A) marginally slowed the pacemaking activity and increased CL

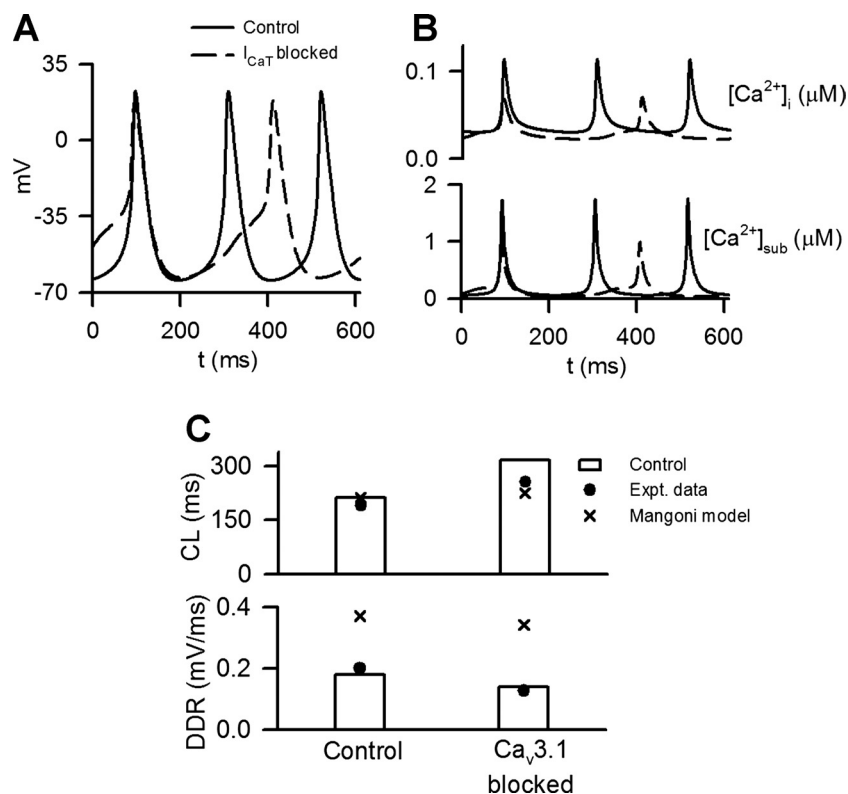


Fig. 6. Functional effects of I_{CaT} block. A: AP profiles under control (solid lines) and I_{CaT} blocked (dashed lines) conditions. B: $[Ca^{2+}]_i$ (top) and $[Ca^{2+}]_{sub}$ (bottom) profiles during APs under control (solid lines) and I_{CaT} blocked (dashed lines) conditions. C: CL (top) and DDR (bottom) under control and I_{CaT} blocked conditions. Shown are the model simulation (open bars), experimental data (●) (56), and Mangoni et al. (56) model simulation data (×).

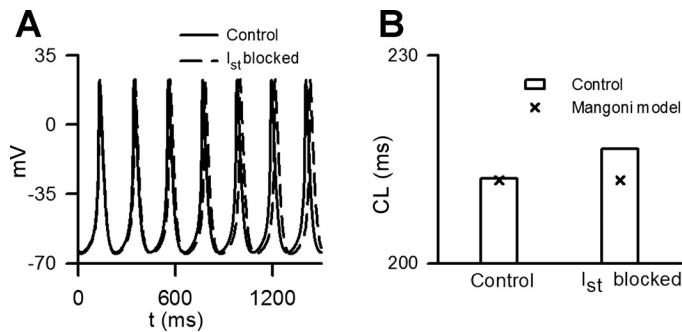


Fig. 7. Functional effects of I_{st} block. **A**: AP profiles under control (solid lines) and I_{st} blocked (dashed lines) conditions in the model. **B**: CL under control and I_{st} blocked conditions. Shown are the basal cell model simulation (open bars) and Mangoni et al. (56) model data (x).

by 2.1%. The alterations in CL due to I_{st} block are shown in Fig. 7B.

Role of I_f . The role of I_f in cardiac pacemaking remains controversial. A recent study (50) has argued the important role of I_f in SAN pacemaking. However, HCN4 gene knockout experimental studies (4, 26) in the mouse SAN have shown that the role of I_f is significant, albeit not isolated from other mechanisms governing pacemaking. The functional role of I_f on mouse SAN pacemaking activity was determined by block of I_f (Fig. 8A). Complete block of I_f slowed down pacemaking, with CL being increased by 13.72% in the model. It produced a more hyperpolarized MDP to -69.4 mV, a hyperpolarization of 5 mV. Since I_f modulates pacemaking by primarily acting during the DDR phase of the AP, it did not affect OS and APD. The measured CL and DDR under complete block conditions are shown in Fig. 8, B and C, respectively. Effects of alterations of g_h on model CL and DDR are shown in Fig. S10.

Role of I_{Kr} . The role of I_{Kr} in the present model is to modulate APD and APA. Partial block of I_{Kr} by 48% prolonged APD₉₀ by 27.96% in the model. Accompanied with APD prolongation, block of I_{Kr} also elevated MDP by $+4.2$ mV in the model. Note that partial block of I_{Kr} only marginally reduced pacemaking (CL increased marginally by $\sim 0.7\%$; Fig. 9A,i). Such a response to I_{Kr} block has been observed experimentally in the rabbit SAN (8) and has also been reproduced in parent rabbit SAN models (37, 89). This is due to the primary function of I_{Kr} being modulation of APD and APA. As I_{Kr} was progressively blocked, APA reduced progressively (Fig. 9, A,ii, and Fig. S11). The reduction in APA is attributable to the elevated MDP, which results in incomplete activation of I_{Na} and I_{CaL} in the upstroke phase, giving reduced APA. Complete block of I_{Kr} abolished the pacemaking activity with V_m resting at -0.35 mV. Upon block of I_{Kr} by 48%, pacemaking in the Mangoni et al. (56) model was abolished.

The present model showed a marginal reduction of CL due to I_{Kr} block, whereas our experimental data (62) showed that application of $1 \mu\text{M}$ E-4031 reduced CL by 68%. In isolated mouse hearts, Cho et al. (10) found that $1 \mu\text{M}$ E-4031 reduced CL by 36.5%. A low ($0.2 \mu\text{M}$) concentration of E-4031 was found to inhibit cellular I_{Kr} in the mouse SAN by 60% and increase CL by 51.5% in the experimental study by Clark et al. (11). In intact mouse hearts, the same study found an application of $1 \mu\text{M}$ E-4031 to increase CL in the range of 31–212%. E-4031 is presumed to be an I_{Kr} -selective drug. However,

Verheijck et al. (79) showed that E-4031 not only inhibits I_{Kr} strongly but also reduces I_{CaL} by 30% in the rabbit SAN. Admittedly, the 30% block of I_{CaL} was observed at a high ($10 \mu\text{M}$) concentration of E-4031. In the present model, a substantial reduction of I_{CaL} (45%) was found to be necessary in the model to give a prolonged CL. Other major K^+ currents (i.e., I_{K1} , I_{to} , I_{Ks} , and I_{sus}) may also be sensitive to E-4031 but were found to play insignificant roles in the model's pacemaking behavior (Fig. S11). Therefore, the effects of E-4031 were simulated by reducing I_{Kr} density by 60% and reducing I_{CaL} density by 50%. As shown in Fig. 9, B,i and ii, such alterations reduced pacemaking by 30.5%. APD₉₀ was prolonged by 87.1%, and dV/dt_{max} was reduced by 79%. The present model as well as previous models (36, 56, 89) cannot reproduce CL prolongation by means of I_{Kr} block alone, which is a possible model limitation. To reproduce E-4031-induced prolongation of CL, reductions of I_{Kr} as well as I_{CaL} are required in the present model. The full effect of E-4031 on mouse SAN ionic currents requires future experimental quantification.

Role of I_{to} . It has been shown experimentally that I_{to} block causes an increase of APA and prolongs APD (40). Selective block of I_{to} in the model increased CL by 3.6% and prolonged APD₅₀ by 10.2% and APD₉₀ by 5.5% (Fig. 9, C,i and ii). Importantly, block of I_{to} caused OS to increase by 7 mV. The effect of I_{to} on OS reflects its role in regulating the early phase of repolarization. The small role of I_{to} in the present SAN cell model could be a model limitation (Fig. S11C). However, it should be noted that the role of I_{to} is greater in modulating repolarization in the ventricles compared with the atria (85, 86) and SAN (64, 65). To date, the biophysical properties of I_{to} in the mouse SAN have not been experimentally quantified. Furthermore, previous SAN modeling studies (36, 50, 89) have indicated that the role of I_{to} , compared with I_{Kr} , in regulating SAN AP characteristics is that of regulating OS and early repolarization. Further experimental quantification of I_{to} properties in mouse SAN cells will improve our understanding of $K_{v4.2}/K_{v4.3}$ I_{to} channels.

Role of I_{NaCa} . I_{NaCa} strongly couples the AP to intracellular Ca^{2+} and contributes to the DDR phase of the SAN AP.

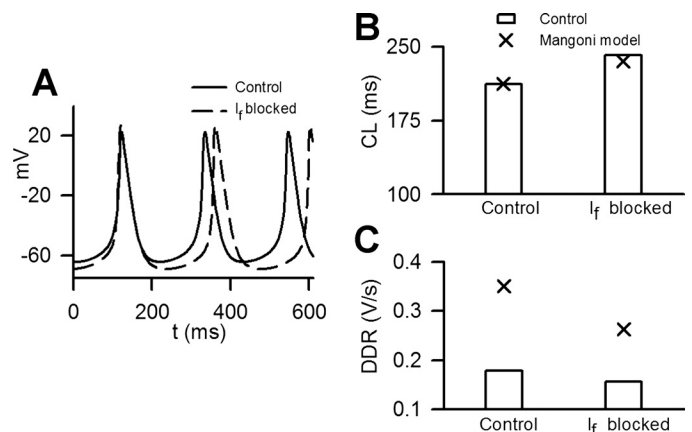


Fig. 8. Functional effects of block of I_f . **A**: AP profiles under control (solid line) and total I_f blocked (dashed line) conditions in the model. **B**: CL under control and I_f blocked conditions. **C**: DDR under control and I_f blocked conditions. Shown are the cell model simulation (open bars) and Mangoni et al. (56) model data (x).

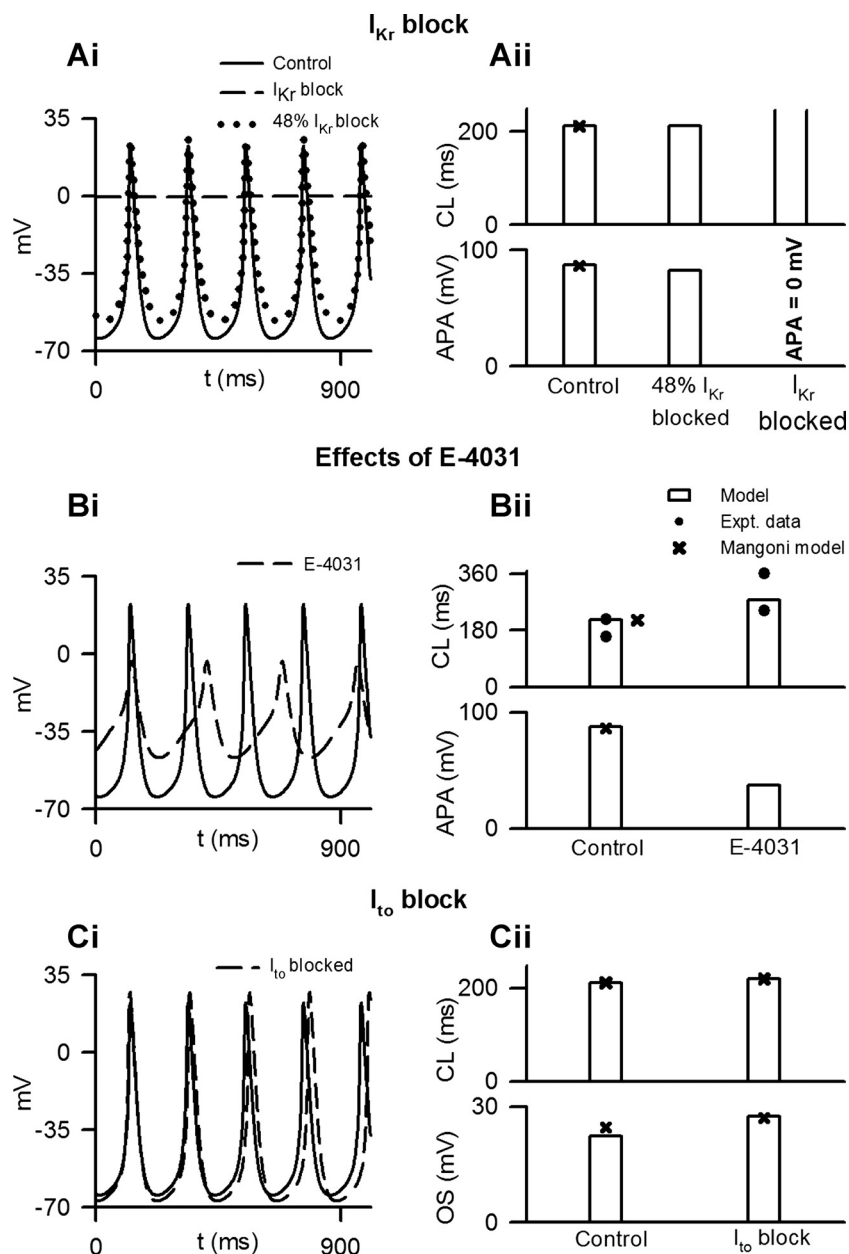


Fig. 9. Role of I_{Kr} , simulated effects of E-4031, and contribution of I_{to} in mouse SAN pacemaking. Solid lines denote control AP profiles, and open bars show present model simulation data. \times , Mangoni et al. (56) model data; \bullet , experimental data. *A.i*: AP profiles under control, partial 48% I_{Kr} blocked (dotted line), and total I_{Kr} blocked (dashed line) conditions in the cell model. *A.ii*: CL (top) and APA (bottom) under control, 48% I_{Kr} blocked, and total I_{Kr} blocked conditions. *B.i*: AP profiles under control and E-4031 (dotted line) conditions in the cell model. *B.ii*: CL (top) and APA (bottom) under control and E-4031 conditions. *C.i*: AP profiles under control and I_{to} blocked (dotted line) conditions in the cell model. *C.ii*: CL (top) and APA (bottom) under control and I_{to} blocked conditions.

Progressive reduction of I_{NaCa} reduced APA and DDR, eventually giving rise to aperiodic or chaotic oscillations. When I_{NaCa} was blocked by $>70\%$, regular pacemaking activity was abolished. Complete block of I_{NaCa} set V_m to a resting value at -39.5 mV (Fig. 10). The effects of various levels of I_{NaCa} inhibition or augmentation on APA and DDR are shown in Fig. S12. With a decrease of I_{NaCa} , APA monotonically decreased. With severe block ($>70\%$), APs became aperiodic and eventually pacemaking was arrested. The I_{NaCa} formulation in the Mangoni et al. (56) model was adopted from the Zhang et al. (89) model. Their formulation of I_{NaCa} does not provide the strong coupling between membrane and intracellular processes. Therefore, although block of I_{NaCa} in the Mangoni et al. (56) model produced a prolonged CL by 18.9%, it is not an essential component of the pacemaking mechanism in their model.

Role of intracellular Ca^{2+} . The role of intracellular Ca^{2+} release and uptake mechanisms was investigated in the model. In the basal model, SR Ca^{2+} SERCA uptake and RyR release mechanisms were based on the formulations by Shannon et al. (73). The isolated Ca^{2+} clock model has been previously investigated in detail (50) and produces a wide range of pacing rates suitable for the rabbit SAN cell model. We further explored the two-parameter space of the uptake rate parameter P_{up} and the release rate parameter k_s to adapt the Ca^{2+} clock to our membrane clock of the mouse SAN cell model. The integrated model was then able to reproduce a wide range of stable CL APs regulated by the intracellular Ca^{2+} -handling mechanism (Fig. 11A). By identifying appropriate values of P_{up} and k_s (shown by “+” in Fig. 11A), the model was able to generate stable pacemaking APs and intracellular Ca^{2+} transients (Fig. 11B). Upon block of SR uptake ($P_{up} = 0$), pace-

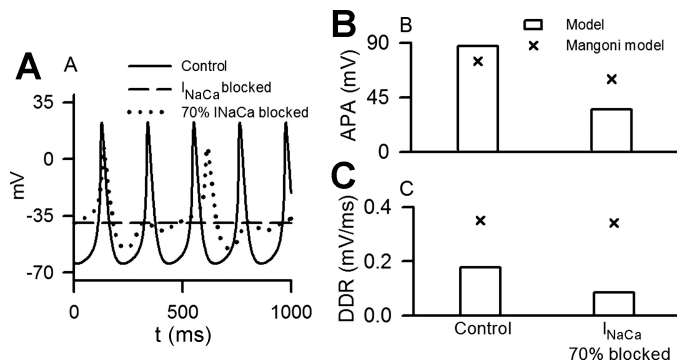


Fig. 10. Effects of I_{NaCa} inhibition on pacemaking activity. A: AP profiles under control (solid line), partial 70% I_{NaCa} blocked (dotted line), and total I_{NaCa} blocked (dashed line) conditions in the model. APA (B) and DDR (C) under control and partial 70% I_{NaCa} blocked conditions. Shown are the model simulation (open bars) and Mangoni et al. (56) model data (\times).

making was dramatically slowed down (Fig. 11C). Ryanodine is known to slow down pacemaking in the mouse SAN (62) by means of challenging SR Ca^{2+} release (9). In the model, block of SR Ca^{2+} release ($k_s = 0$) also had a severe effect on the AP, making it aperiodic (Fig. 11D). Furthermore, when intracellular Ca^{2+} ($[Ca^{2+}]_{sub}$ and $[Ca^{2+}]_i$) was buffered to diastolic concentrations ($[Ca^{2+}]_i$ and $[Ca^{2+}]_{sub}$ set to 50 nM, simulating the effects of BAPTA), pacemaking was arrested (Fig. 11E).

Effects of Iso on mouse SAN pacemaking activity. The adrenergic response of the pacemaking mechanism in the mouse SAN has been studied using Iso experimentally. It has been shown that Iso causes a positive shift of the $V_{1/2}$ of I_f . Alig et al. (1) observed a shift from -106 to -92 mV (a positive shift of $+14$ mV). Baruscotti et al. (4) saw a similar $+7$ -mV shift, whereas Liao et al. (43) saw a shift from -128 to -110 mV (shift of $+18$ mV). The slope factors in the steady-state of activation were unaffected. Upon shift of the $V_{1/2}$ from -106 to -92 mV in our model, CL was marginally reduced (CL = 208.1 ms). The effects of varied $V_{1/2}$ and P_{up} on model pacemaking are shown in Fig. S13. As the simulated effect of shift of $V_{1/2}$ was substantially smaller than the experimentally observed effects of the 20–40% increase in pacemaking rates (1, 4, 84), it might implicate a possible role of changes in the intracellular Ca^{2+} mechanism and other ionic currents affected by Iso. Experimentally, it has been found that I_{CaL} is dramatically affected by Iso, resulting in augmented I_{CaL} density (1) as well as a shift of the $I-V$ curve to more negative potentials (72). Similarly, Iso also augments I_{Kr} density (by 12%) and shifts its steady state of activation to more negative potentials (82). Experimentally, it has also been observed that Iso increased I_{NaK} activity by increasing its sensitivity to $[Na^+]_i$ (5, 15, 23), i.e., a reduction of the half-maximal $[Na^+]_i$ in I_{NaK} ($K_{m,Na}$). Iso also augmented SR uptake and release by stimulation of Ca^{2+} /calmodulin-dependent protein kinase II (50, 73). In simulations of Iso, we adopt the approach of Shannon et al. (72) and reduced the $[Ca^{2+}]_i$ affinity of the forward model of the SERCA pump (K_{mf}) and increased the baseline non-SR-dependent transition rate constant of RyR (K_{oCa}) in the Ca^{2+} release mechanism. Therefore, in accordance with experimental data, the effects of Iso were simulated by the following: 1) shift of I_f $V_{1/2}$ to -92 mV (1); 2) increasing current densities of both I_{CaL} isoforms by 45% (1); 3) shift of the I_{CaL} $I-V$ curves toward more negative potentials by 5 mV (72); 4) reducing

$K_{m,Na}$ from 14 to 11 mM (5, 15); 5) augmenting g_{Kr} by 12% (82); 6) shift of the I_{Kr} steady state of activation by 5 mV to more negative potentials (82); 7) reducing K_{mf} from 0.246 to 0.123 μ M (72); and 8) increasing K_{oCa} from 10 to 20 mM^{-2}/ms (72). With these changes, simulated APs and Ca^{2+} transients under control and Iso conditions are shown in Fig. 12, A and B. Simulated actions of Iso produced a 23.21% reduction of CL (CL = 163.1 ms; Fig. 12C). Along with the reduced CL, there was an increase in the $[Ca^{2+}]_{sub}$ amplitude but a decrease in the amplitude of the cytosolic $[Ca^{2+}]_i$ oscillations. In previous ventricular cell modeling studies (17, 19, 72), $[Ca^{2+}]_i$ has been shown to be augmented due to Iso. $[Ca^{2+}]_i$ is important in the ventricles for tension-force generation (17, 73). In the SAN, however, $[Ca^{2+}]_{sub}$, rather than $[Ca^{2+}]_i$, has been identified to play a more critical role in regulating pacemaking activity (9, 50, 51). With the above-detailed Iso-induced electrophysiological alterations, the Maltsev and Lakatta (50) model also showed a reduction of cytosolic free $[Ca^{2+}]_i$ and an increase of $[Ca^{2+}]_{sub}$. The differences in intracellular compartments and major currents between ventricular and pacemaking cells may explain such a difference between the two cells' responses of $[Ca]_i$ to Iso.

DISCUSSION

The presented model successfully reproduced physiological mouse SAN pacemaking APs with the atypically short APD

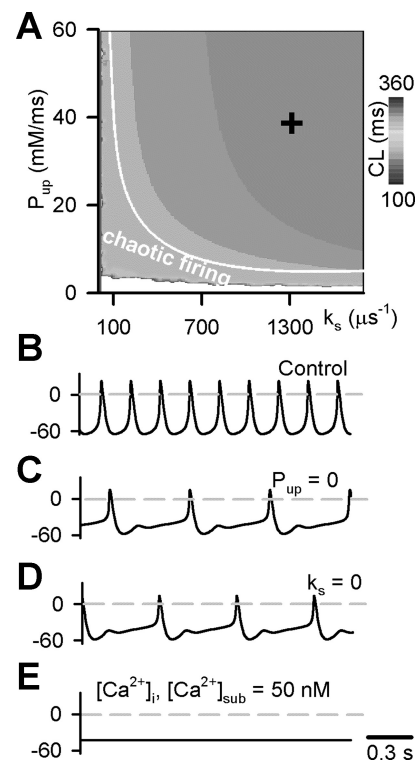


Fig. 11. Regulation of pacemaking by intracellular Ca^{2+} mechanisms. A: parametric analysis of basal cell firing as a function of major intracellular Ca^{2+} parameters for Ca^{2+} uptake (P_{up}) and Ca^{2+} release (k_s). The “+” shows the parameter values used in the basal model. At low P_{up} or low k_s , firing was found to be aperiodic or arrested. In B–D, the dashed gray line shows the 0-mV reference voltage. B: control APs. C: APs under $P_{up} = 0$ conditions. D: APs under $k_s = 0$ conditions. E: APs under Ca^{2+} buffered at diastolic concentrations of 50 nM.

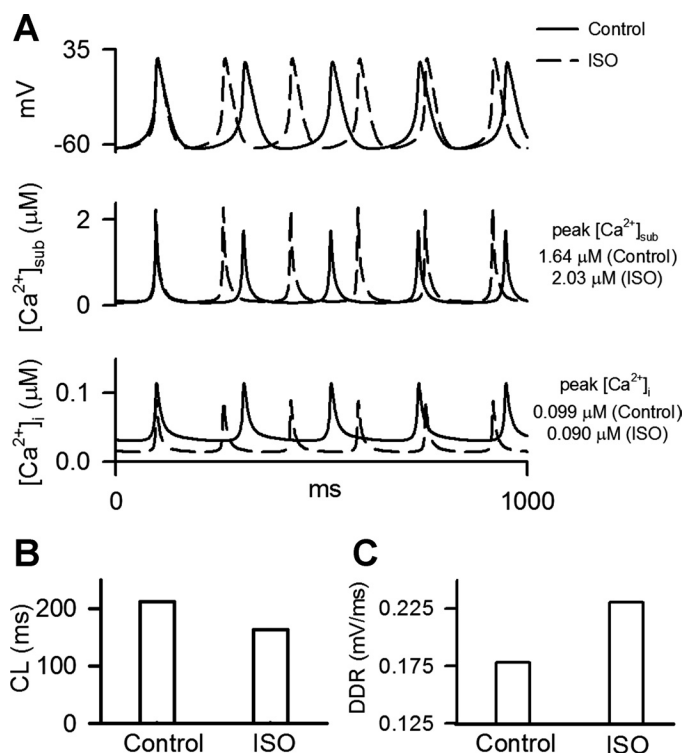


Fig. 12. Effects of Iso. A: solid lines denote control, whereas dashed lines denote Iso simulations. Shown are simulated control AP (top), $[Ca^{2+}]_{sub}$ (middle), and $[Ca^{2+}]_i$ (bottom) profiles. B: CL under control (CL = 212.21 ms) and Iso (CL = 163.59 ms) simulations. C: DDR under control (DDR = 0.178 mV/ms) and Iso (DDR = 0.23 mV/ms) conditions.

and high pacing rate, similar to experimental recordings (39, 41, 55, 56). The model was validated by its ability to reproduce the effects of several ion channel blocks or reduced current density due to gene knockouts as well as intracellular Ca^{2+} alterations on pacemaking APs (10, 25, 52, 55, 56). Its robustness was verified by means of two-parameter analyses. The model thus provides a tool for quantitatively evaluating the functional role of isoform-specific ion channel current on the generation and control of cardiac rhythm. Almost all contemporary SAN models simulate rabbit or guinea pig cell electrical activities, which have substantially different AP morphologies. In a previous study, Mangoni et al. (56) developed a model for the mouse SAN cell AP. However, the simulated APs have a long plateau and APD, a low OS, and a much larger DDR compared with experimental data (Fig. 3). The ionic currents in the Mangoni et al. model (56) were not validated against experimental data either. For example, their $I_{Na,1.1}$ and $I_{Na,1.5}$ models do not reproduce the experimental $I-V$ data of the mouse SAN (41); the $V_{1/2}$ of the steady-state I_f activation curve is positive compared with experimental data (10, 55, 66). In their model, I_{CaL} does not have Ca^{2+} -dependent inactivation, thus limiting the coupling between intracellular ionic concentrations and the pacemaking APs. Assuming constant values for intracellular ion concentrations, I_{NaCa} and I_{NaK} in the Mangoni et al. (56) model are analogs to background currents without functional relevance. Indeed, I_{NaCa} in the model has a much smaller effect on the pacemaking (increase of CL by 18.9% upon block of I_{NaCa}). Since intracellular Ca^{2+} dynamics were not incorporated, the model

offers limited possibilities of studying the regulatory effects advanced mechanisms, such as that of the Ca^{2+} clock (50), on pacemaking. We therefore believe the present biophysically detailed model to be one of the first to reproduce the mouse SAN AP along with the functional roles of ionic currents and intracellular Ca^{2+} handling.

Comparison With Previous Models of Other Species

In recent decades, several mathematical models of the SAN AP have been developed for the rabbit (13, 16, 36, 89) and guinea pig (67). These models are based on a single channel voltage-clamp experimental data representing generic-type ion channels, without considering the species-specific and isoform-specific properties of the ion channels. Although these models provide useful tools to study the functional roles of a certain generic-type ion channel current, they are not suitable to evaluate the functional roles of isoform-specific channels on cardiac pacemaking. The present models have a similar structure to previous SAN models (13, 16, 36, 89) but incorporate the following major difference and important advances.

A major difference between the previous rabbit SAN models and the present mouse model is that the mouse AP has much faster pacemaking rates, a higher OS, and a larger dV/dt_{max} , which are attributable to the emergent interactions of ion channel properties specific to the mouse SAN, e.g., a substantially larger I_{CaL} density in the mouse model and a greater I_{CaT} density than that of I_{CaL} , as found by Mangoni et al. (53).

A major advance in the present model is the introduction of isoform-specific models for the major ionic channel currents present in the SAN, which include I_{Na} (consisting of $I_{Na,1.1}$ and $I_{Na,1.5}$), I_{CaL} (consisting of $I_{CaL,1.2}$ and $I_{CaL,1.3}$), I_{CaT} (consisting of $I_{CaT,3.1}$). Model equations and related parameters for these isoform-specified ion channel currents were based on experimental data measured from mouse SAN cells (2, 10, 11, 26, 41, 52, 55, 56, 66). Another advance is its ability to reproduce the experimentally observed effects of ion channel blockers or gene knockouts (I_{Na} , I_{CaL} , I_{CaT} , I_{Kr} , and I_f) on pacemaking APs of the mouse SAN (11, 39, 41, 52, 56).

Key Achievements of the New Model

A key achievement of the present model is that the simulated APs (Fig. 3) were comparable with those recorded from mouse SAN cells in terms of AP characteristics, including CL, APD₅₀, APD₉₀, OS, MDP, dV/dt_{max} , TOP, and DDR (see Table 3). These models could reproduce experimental data of voltage clamp for some major currents (Figs. S1–S5) as well as the functional roles of isoform-specific channels of I_{Na} and I_{CaL} , which were more accurate than those by the previous Mangoni et al. (56) model. The functional roles of I_{Kr} and I_{to} have been explored in the model and indicate future directions of experimental quantification of mouse SAN electrophysiology. The simulated functional roles of all other channels also matched experimental data (see RESULTS and Figs. 3–11). The model also incorporated an intracellular Ca^{2+} handling mechanism including the Ca^{2+} clock, which, together with the membrane clock, allows the simulation of various experimentally observed findings regarding intracellular Ca^{2+} . Therefore, the present model provides a basis for further simulating the initiation and conduction of cardiac pacemaking activity in the intact tissue of the mouse SAN and atrium in the future.

Limitations of the Model

Limitations of model components. In the model, the functional effects of $I_{Na,1.1}$ (Fig. 4) and $I_{CaL,1.2}$ (Fig. 5) were limited. This is partly due to the window currents of both these isoforms being small compared with other dominant isoforms (Figs. S1 and S2). Furthermore, these window currents line in the diastolic depolarization phase of the AP, where I_{NaCa} , I_f , and intracellular Ca^{2+} mechanisms play a predominant role. The biophysical properties of these isoforms will be improved as experimental data become available. A second limitation of the model is that I_{Kr} block did not affect pacemaking rates, in contrast to our experimental observations. In most contemporary models of the SAN, I_{Kr} block causes increased pacemaking along with a reduction of APA. This limitation may be due to the inadequate modeling of I_{Kr} using a Hodgkin-Huxley formulation (36), as stated below. The modeling of I_{Kr} and I_{CaT} can also be further improved when more experimental data on their biophysical properties become available. Finally, the intracellular Ca^{2+} mechanism did not modulate pacemaking as strongly in the present model compared with the study of Maltsev and Lakatta (50). Although block of SR uptake or release showed the experimentally observed alterations in pacemaking, the augmentation of P_{up} in the present model had a smaller effect compared with the rabbit model (50). This is a consequence of the large current densities of I_{CaL} , I_{CaT} , and I_f . Furthermore, the present model consisted of ionic currents I_{Na} and I_{K1} , which are absent in the model of Maltsev and Lakatta (50), which also contributes the differences in the functional roles of Ca^{2+} clocks between the two models. The role of the Ca^{2+} clock in SAN pacemaking is still under debate (27), and further experimental quantification of SAN cellular intracellular mechanisms is definitely required.

Lack of complete experimental data. There is a lack of a complete data set on ion channel gating and kinetics, especially the intracellular Ca^{2+} handling mechanisms from the mouse SAN. In model development, we considered mouse SAN-specific biophysical data for some major currents but implemented generic current models for other channel currents (Table S1), which either have a small effect (e.g., I_{Ks}) or are primarily fine tuning tools for the model development (e.g., I_{NaK} and background currents). Although the mouse is a widely used animal model in the study of SAN and atrial arrhythmias, the quantification of the biophysical properties of mouse membrane electrophysiology is still limited. In some instances, we need to use data obtained either at low temperature or from different species. Uncertainty about the accuracy of the experimental data further limited model functionality. The models also do not include some currents known to play important roles in the mouse SAN, for example, ACh-activated K^+ current (18, 47), ATP-sensitive K^+ current (18), a Ca^{2+} -activated nonselective cationic current (12), and store-activated Ca^{2+} channel currents (30).

Model limitations due to Hodgkin-Huxley ion currents and lack of the Ca^{2+} sparks. Hodgkin-Huxley formulation as basis of ion channel currents and passive diffusion of intracellular Ca^{2+} have already been shown to be limiting factors for mathematical models of cardiac APs (50). For the ion channel currents, two-state Hodgkin-Huxley formulation cannot faithfully simulate the activation, inactivation, and deactivation process as a multistate Markovian chain formulation does.

However, the Markovian chain formulation requires extensive experimental data obtained at various protocols for validating model parameters. Otherwise, the parameter set may not be unique. To our best knowledge, such experimental data necessary for developing a well-validated Markovian chain model for mouse SAN ion channels are not yet unavailable. Therefore, two-state Hodgkin-Huxley formulation was implemented in the present models.

Ca^{2+} diffusion from the subspace to the myoplasm, Ca^{2+} release and uptake by the SR, and Ca^{2+} buffering mechanisms were adopted from the parent Kurata et al. (37) model and from Shannon et al. (73). It allowed simulation of the experimentally observed effects of Ca^{2+} /calmodulin-dependent protein kinase II, cyclopiazonic acid, and RyRs (38, 48–50). Investigating the role of Ca^{2+} sparks in driving SAN cell pacemaking due to the lack of spatially extended considerations of Ca^{2+} dynamics, as done in our recent study (76), would be the next modeling challenge.

Despite these limitations, the models presented here represent a significant progress in developing biophysically detailed mathematical models for mouse SAN cells and form a basis for further development with the advent of new experimental data.

Conclusions

In this study, a mathematical model for pacemaking APs of the mouse SAN cell has been developed. This model forms an important step leading toward a “virtual whole heart” of the mouse. Using the model, we analyzed the functional role of individual ion channel currents and intracellular Ca^{2+} handling on generating mouse pacemaking APs. Our simulation data have shown that the genesis of pacemaking APs is a coordinated action of all ion channel currents (involving both depolarizing and repolarizing currents) and the intracellular Ca^{2+} clock, rather than being regulated by a single factor. For example, block of inward depolarizing currents, such as I_{Na} , I_f , I_{CaT} , I_{st} , or I_{NaCa} , slowed down pacemaking APs, highlighting their functional contributions to mouse SAN pacemaking APs. Block of outward repolarizing current, such as I_{Kr} , abolished the pacemaking AP, indicating its important role as well. In the present model, intracellular Ca^{2+} handling has been shown to contribute to pacemaking APs (50) but does not underestimate the importance of HCN-related ionic pacemaking mechanisms (4).

APPENDIX: MODEL EQUATIONS

Membrane Potential

$$dV/dt = -(I_{Na,1.1} + I_{Na,1.5} + I_{CaL,1.2} + I_{CaL,1.3} + I_{CaT} + I_{Kr} + I_{Ks} + I_f + I_{to} + I_{sus} + I_{K1} + I_{st} + I_{NaK} + I_{NaCa} + I_{b,Na} + I_{b,K} + I_{b,Ca})/C_m$$

Gating Variables

$$dg/dt = (g_{\infty} - g)/\tau_g \text{ for any gating variable } g \text{ with steady-state value } g_{\infty}$$

Reversal Potentials

$$E_K = (RT/F)\ln([K^+]_o/[K^+]_i)$$

$$E_{Na} = (RT/F)\ln([Na^+]_o/[Na^+]_i)$$

$$E_{Ca} = (RT/2F)\ln([Ca^{2+}]_o/[Ca^{2+}]_{sub})$$

$$E_{Ks} = (RT/F)\ln([K^+]_o + 0.12[Na^+]_o)/([K^+]_i + 0.12[Na^+]_i)$$

$I_{Na,1.1}$ and $I_{Na,1.5}$

$$I_{Na,1.1} = g_{Na,1.1} m_{1.1}^3 h_{1.1} [Na^+]_o V [e^{(V \cdot E_{Na})/RT} - 1] / (e^{V/RT} - 1) F^2 / (RT)$$

$$I_{Na,1.5} = g_{Na,1.5} m_{1.5}^3 h_{1.5} [Na^+]_o V [e^{(V \cdot E_{Na})/RT} - 1] / (e^{V/RT} - 1) F^2 / (RT)$$

$$m_{1.1\infty} = 1 / [1 + e^{-(V+31)/5}]^{1/3}$$

$$h_{1.1\infty} = 1 / [1 + e^{(V+56)/3}]$$

$$j_{1.1\infty} = h_{1.1\infty}$$

$$m_{1.5\infty} = 1 / [1 + e^{-(V+45.214)/7.220}]^{1/3}$$

$$h_{1.5\infty} = 1 / [1 + e^{(V+62.578)/6.084}]$$

$$j_{1.5\infty} = h_{1.5\infty}$$

$$F_{Na} = 0.0952 e^{-0.063(V+34.4)} / [1 + 1.66 e^{-0.225(V+63.7)}] + 0.0869$$

$$h_{1.1} = (1 - F_{Na}) h_{1.1} + F_{Na} j_{1.1}$$

$$h_{1.5} = (1 - F_{Na}) h_{1.5} + F_{Na} j_{1.5}$$

$$\tau_m = 0.6247 / [0.832 e^{-(V+46.7)/2.985} + 0.6274 e^{(V+55.01)/12.195}] + 0.04569$$

$$\tau_h = 0.113 \{ 1 / [13475.066 e^{(V-59.398)/15.645}] + 1 / [1.113 + 0.044 e^{-(V-86.768)/8.059}] \}^{-1}$$

$$\tau_j = 0.125 \{ 1 / [140557.232 e^{(V-59.455)/17.380}] + 1 / [2.471 + 0.767 e^{-(V-68.931)/18.237}] \}^{-1}$$

 $I_{CaL,1.2}$ and $I_{CaL,1.3}$

$$I_{CaL,1.2} = g_{CaL,1.2} d_{L,1.2} f_{L,1.2} f_{Ca}(V - E_{CaL})$$

$$I_{CaL,1.3} = g_{CaL,1.3} d_{L,1.3} f_{L,1.3} f_{Ca}(V - E_{CaL})$$

$$d_{L,1.2\infty} = 1 / [1 + e^{-(V+3)/5}]$$

$$f_{L,1.2\infty} = 1 / [1 + e^{(V+36)/4.6}]$$

$$d_{L,1.3\infty} = 1 / [1 + e^{-(V+13.5)/6}]$$

$$f_{L,1.3\infty} = 1 / [1 + e^{(V+35)/4.1}]$$

$$\alpha_{d_L} = -28.39(V+35) / [e^{-(V+35)/2.5} - 1] - 84.9V / (e^{-0.208V} - 1)$$

$$\beta_{d_L} = 11.43(V-5) / [e^{0.4(V-5)} - 1]$$

$$\tau_{d_L} = 2,000 / (\alpha_{d_{L,1.3}} + \beta_{d_{L,1.3}})$$

$$\tau_{f_{L,1.2}} = 7.485 + 45.774 e^{-0.5[(V+24.753)/13]^2}$$

$$\tau_{f_{L,1.3}} = 7.485 + 45.774 e^{-0.5[(V+28.753)/11]^2}$$

$$f_{Ca\infty} = K_{mf_{Ca}} / (K_{mf_{Ca}} + [Ca^{2+}]_{sub})$$

$$\tau_{f_{Ca}} = f_{Ca\infty} / \alpha_{f_{Ca}}$$

 I_{CaT}

$$I_{CaT} = g_{CaT} d_{Tf}(V - E_{CaT})$$

$$d_{T\infty} = 1 / [1 + e^{-(V+26)/6}]$$

$$\tau_{d_T} = 1 / [1.068 e^{(V+26.3)/30} + 1.068 e^{-(V+26.3)/30}]$$

$$f_{T\infty} = 1 / [1 + e^{(V+61.7)/5.6}]$$

$$\tau_{f_T} = 1 / [0.0153 e^{-(V+61.7)/83.3} + 0.015 e^{(V+61.7)/15.38}]$$

 I_{Kr}

$$I_{Kr} = g_{Kr} p_a p_i (V - E_K)$$

$$p_{a\infty} = 1 / [1 + e^{-(V+21.174)/9.757}]$$

$$\tau_{Pa} = 0.7 / (0.003596 e^{V/15.33} + 0.000177 e^{-V/25.868})$$

$$p_{i\infty} = 1 / [1 + e^{(V+28.6)/17.1}]$$

$$\tau_{Pi} = 0.2 + 0.9 / (0.1 e^{V/54.645} + 0.656 e^{V/106.157})$$

 I_{Ks}

$$I_{Ks} = g_{Ks} x_s^2 (V - E_{Ks})$$

$$x_{s\infty} = 1 / [1 + e^{-(V-20.876)/11.853}]$$

$$\tau_{Pa} = 1,000 \{ 13.098 / [1 + e^{-(V-48.911)/10.630}] + e^{-V/35.317} \}^{-1}$$

 I_f

$$I_f = I_{fNa} + I_{fK}$$

$$I_{fNa} = 0.3833 g_{hy}(V - E_K)$$

$$I_{fK} = 0.6167 g_{hy}(V - E_{Na})$$

$$y_i = 1 / [1 + e^{(V+106.8)/16.3}]$$

$$\tau_y = 1.505 / [e^{-0.011(V+590.3)} + e^{(V+85.1)/17.2}]$$

 I_{st}

$$I_{st} = g_{st} q_a q_i (V - E_{st})$$

$$q_{a\infty} = 1 / [1 + e^{-(V+67)/5}]$$

$$\alpha_{q_a} = 1 / (0.15 e^{-V/11} + 0.2 e^{-V/700})$$

$$\beta_{q_a} = 1 / (16 e^{V/18} + 15 e^{V/50})$$

$$\tau_{q_a} = 1 / (\alpha_{q_a} + \beta_{q_a})$$

$$\alpha_{q_i} = 0.15 / [3,100 e^{(V+10)/13} + 700 e^{(V+10)/70}]$$

$$\beta_{q_i} = 0.15 / [95.7 e^{-(V+10)/10} + 50 e^{-(V+10)/700}] + 0.000229 / [1 + e^{-(V+10)/5}]$$

$$q_{i\infty} = \alpha_{q_i} / (\alpha_{q_i} + \beta_{q_i})$$

$$\tau_{q_i} = 1 / (\alpha_{q_i} + \beta_{q_i})$$

 I_{K1}

$$I_{K1} = g_{K1} [K^+]_o (V - E_K) / \{ [1 + e^{0.071(V-E_K)}] ([K^+]_o + 0.229) \}$$

 I_{to} and I_{sus}

$$I_{to} = g_{to} r q (V - E_K)$$

$$I_{sus} = g_{sus} r (V - E_K)$$

$$r_{\infty} = 1 / [1 + e^{-(V-19.3)/15}]$$

$$\tau_r = 9 + 47.52 / [1.037 e^{0.08(V+30.61)} + 0.369 e^{-0.12(V+23.84)}]$$

$$q_{\infty} = 1 / [1 + e^{(V+49)/13}]$$

$$\tau_q = 6.06 + 39.1 / [0.57 e^{-0.08(V+44)} + 0.065 e^{0.1(V+45.93)}]$$

 I_{NaK}

$$I_{NaK} = \overline{I_{NaK}} [1 + (K_{mKp} / [K^+]_o)^{1.2}]^{-1} [1 + (K_{mNap} / [Na^+]_i)^{1.3}]^{-1} [1 + e^{-(V_m - E_{Na} + 120)/30}]^{-1}$$

 I_{NaCa}

$$I_{NaCa} = k_{NaCa} (k_{21} x_2 - k_{12} x_1) / (x_1 + x_2 + x_3 + x_4)$$

$$d_i = 1 + ([Ca^{2+}]_{sub} / K_{ci}) (1 + e^{-Q_{ci} V / RT} + [Na^+]_i / K_{cni}) + ([Na^+]_i / K_{1ni}) [(1 + [Na^+]_i / K_{2ni}) (1 + [Na^+]_i / K_{3ni})]$$

$$d_o = 1 + ([Ca^{2+}]_o / K_{co}) (1 + e^{Q_{co} V / RT}) + ([Na^+]_o / K_{1no}) [1 + ([Na^+]_o / K_{2no}) (1 + [Na^+]_o / K_{3no})]$$

$$k_{43} = [Na^+]_i / (K_{3ni} + [Na^+]_i)$$

$$k_{12} = ([Ca^+]_{sub} / K_{ci}) e^{-Q_{ci} V / RT} / d_i$$

$$k_{14} = ([Na^+]_i / K_{1ni}) ([Na^+]_i / K_{2ni}) (1 + [Na^+]_i / K_{3ni}) e^{-Q_n V / 2RT} / d_i$$

$$k_{41} = e^{-Q_n V / 2RT}$$

$$\begin{aligned}
 k_{34} &= [\text{Na}^+]_o / (K_{3no} + [\text{Na}^+]_o) \\
 k_{21} &= ([\text{Ca}^{2+}]_o / K_{co}) e^{Q_{co} V_F / RT} / d_o \\
 k_{23} &= ([\text{Na}^+]_o / K_{1no}) ([\text{Na}^+]_o / K_{2no}) (1 + [\text{Na}^+]_o / K_{3no}) e^{Q_n V_F / 2RT} / d_o \\
 k_{32} &= e^{Q_n V_F / 2RT} \\
 x_1 &= k_{34} k_{41} (k_{23} + k_{21}) + k_{21} k_{32} (k_{43} + k_{41}) \\
 x_2 &= k_{43} k_{32} (k_{14} + k_{12}) + k_{41} k_{12} (k_{34} + k_{32}) \\
 x_3 &= k_{43} k_{14} (k_{23} + k_{21}) + k_{12} k_{23} (k_{43} + k_{41}) \\
 x_4 &= k_{34} k_{23} (k_{14} + k_{12}) + k_{21} k_{14} (k_{34} + k_{32})
 \end{aligned}$$

$I_{b,Na}$, $I_{b,K}$, and $I_{b,Ca}$

$$\begin{aligned}
 I_{b,Na} &= g_{b,Na} (V - E_{Na}) \\
 I_{b,K} &= g_{b,K} (V - E_K) \\
 I_{b,Ca} &= g_{b,Ca} (V - E_{Ca})
 \end{aligned}$$

Ca^{2+} Handling

Ca^{2+} handling in the SR.

$$\begin{aligned}
 j_{up} &= P_{up} \frac{([\text{Ca}^{2+}]_i / K_{mf})^{n_{up}} - ([\text{Ca}^{2+}]_{up} / K_{mr})^{n_{up}}}{1 + ([\text{Ca}^{2+}]_i / K_{mf})^{n_{up}} + ([\text{Ca}^{2+}]_{up} / K_{mr})^{n_{up}}} \\
 j_{tr} &= ([\text{Ca}^{2+}]_{up} - [\text{Ca}^{2+}]_{rel}) / \tau_{tr} \\
 j_{rel} &= k_s O ([\text{Ca}^{2+}]_{rel} - [\text{Ca}^{2+}]_{sub})
 \end{aligned}$$

$$k_{CaSR} = \text{MaxSR} - (\text{MaxSR} - \text{MinSR}) / [1 + (\text{EC}_{50_SR} / [\text{Ca}^{2+}]_{rel})^{\text{HSR}}]$$

$$k_{oSRCa} = k_{oCa} / k_{CaSR}$$

$$k_{iSRCa} = k_{iCa} \times k_{CaSR}$$

$$\begin{aligned}
 dO/dt &= (k_{oSRCa} \times [\text{Ca}^{2+}]_{sub}^2 R - k_{om} \times O) \\
 &\quad - (k_{iSRCa} \times [\text{Ca}^{2+}]_{sub} \times O - k_{im} \times I)
 \end{aligned}$$

$$\begin{aligned}
 dI/dt &= (k_{iSRCa} \times [\text{Ca}^{2+}]_{sub} O - k_{im} \times I) \\
 &\quad - (k_{om} \times I - k_{oSRCa} \times [\text{Ca}^{2+}]_{sub}^2 \times RI)
 \end{aligned}$$

$$\begin{aligned}
 dR/dt &= (k_{im} \times RI - k_{iSRCa} \times [\text{Ca}^{2+}]_{sub} \times R) \\
 &\quad - (k_{oSRCa} \times [\text{Ca}^{2+}]_{sub}^2 R - k_{om} \times O)
 \end{aligned}$$

$$\begin{aligned}
 dRI/dt &= (k_{om} \times I - k_{oSRCa} \times [\text{Ca}^{2+}]_{sub}^2 \times RI) \\
 &\quad - (k_{im} \times RI - k_{iSRCa} \times [\text{Ca}^{2+}]_{sub} \times R)
 \end{aligned}$$

Ca^{2+} diffusion.

$$j_{Ca,dif} = ([\text{Ca}^{2+}]_{sub} - [\text{Ca}^{2+}]_i) / \tau_{Ca,dif}$$

Intracellular ionic concentrations.

$$\begin{aligned}
 d[\text{Ca}^{2+}]_i/dt &= (j_{Ca,dif} V_{sub} - j_{up} V_{up}) / V_i - ([\text{CM}]_{tot} df_{CMi}/dt \\
 &\quad + [\text{TC}]_{tot} df_{TC}/dt + [\text{TMC}]_{tot} df_{TMC}/dt)
 \end{aligned}$$

$$\begin{aligned}
 d[\text{Ca}^{2+}]_{sub}/dt &= [-(I_{CaL,1.2} + I_{CaL,1.3} + I_{CaT} + I_{b,Ca} - 2I_{NaCa}) / 2F \\
 &\quad + j_{rel} V_{rel}] / V_{sub} - j_{Ca,dif} - [\text{CM}]_{tot} df_{CMs}/dt
 \end{aligned}$$

$$d[\text{Ca}^{2+}]_{rel}/dt = j_{tr} - j_{rel} - [\text{CQ}]_{tot} df_{CQ}/dt$$

$$d[\text{Ca}^{2+}]_{up}/dt = j_{up} - j_{tr} V_{rel} / V_{up}$$

$$\begin{aligned}
 d[\text{Na}^+]_i/dt &= -(I_{b,Na} + I_{Na,1.1} + I_{Na,1.5} + 3I_{NaK} \\
 &\quad + 3I_{NaCa} + I_{st} + I_{b,Na}) / FV_i
 \end{aligned}$$

$$\begin{aligned}
 d[\text{K}^+]_i/dt &= -(I_{b,K} + I_{Ks} + I_{Kr} + I_{K1} + I_{b,K} \\
 &\quad - 2I_{NaK} + I_{sus} + I_{to}) / FV_i
 \end{aligned}$$

Ca^{2+} buffering.

$$df_{TC}/dt = k_{f_{TC}} [\text{Ca}^{2+}]_i (1 - f_{TC}) - k_{b_{TC}} f_{TC}$$

$$df_{TMC}/dt = k_{f_{TMC}} [\text{Ca}^{2+}]_i (1 - f_{TMC} - f_{TMM}) - k_{b_{TMC}} f_{TMC}$$

$$df_{TMM}/dt = k_{f_{TMM}} [\text{Mg}^{2+}]_i (1 - f_{TMC} - f_{TMM}) - k_{b_{TMM}} f_{TMM}$$

$$df_{CMi}/dt = k_{f_{CM}} [\text{Ca}^{2+}]_i (1 - f_{CMi}) - k_{b_{CM}} f_{CMi}$$

$$df_{CMs}/dt = k_{f_{CM}} [\text{Ca}^{2+}]_{sub} (1 - f_{CMs}) - k_{b_{CM}} f_{CMs}$$

$$df_{CQ}/dt = k_{f_{CQ}} [\text{Ca}^{2+}]_{rel} (1 - f_{CQ}) - k_{b_{CQ}} f_{CQ}$$

GRANTS

This work was supported by Wellcome Trust (UK) Grant WT/081809/Z/06/Z.

DISCLOSURES

No conflicts of interest, financial or otherwise, are declared by the author(s).

REFERENCES

1. Alig J, Marger L, Mesirca P, Ehmke H, Mangoni ME, Isbrandt D. Control of heart rate by cAMP sensitivity of HCN channels. *Proc Natl Acad Sci USA* 106: 12189–12194, 2009.
2. Altomare C, Terragni B, Brioschi C, Milanese R, Pagliuca C, Viscomi C, Moroni A, Baruscotti M, DiFrancesco D. Heteromeric HCN1-HCN4 channels: a comparison with native pacemaker channels from the rabbit sinoatrial node. *J Physiol* 549: 347–359, 2003.
3. Barbuti A, DiFrancesco D. Control of cardiac rate by “funny” channels in health and disease. *Ann NY Acad Sci* 1123: 213–223, 2008.
4. Baruscotti M, Bucci A, Viscomi C, Mandelli G, Consalez G, Gnechchi-Rusconi T, Montano N, Casali KR, Micheloni S, Barbuti A, DiFrancesco D. Deep bradycardia and heart block caused by inducible cardiac-specific knockout of the pacemaker channel gene Hcn4. *Proc Natl Acad Sci USA* 108: 1705–1710, 2010.
5. Berry RG, Despa S, Fuller W, Bers DM, Shattock MJ. Differential distribution and regulation of mouse cardiac Na^+/K^+ -ATPase α_1 and α_2 subunits in T-tubule and surface sarcolemmal membranes. *Cardiovasc Res* 73: 92–100, 2007.
6. Bogdanov KY, Maltsev VA, Vinogradova TM, Lyashkov AE, Spurgeon HA, Stern MD, Lakatta EG. Membrane potential fluctuations resulting from submembrane Ca^{2+} releases in rabbit sinoatrial nodal cells impart an exponential phase to the late diastolic depolarization that controls their chronotropic state. *Circ Res* 99: 979–987, 2006.
7. Bohn G, Moosmang S, Conrad H, Ludwig A, Hofmann F, Klugbauer N. Expression of T- and L-type calcium channel mRNA in murine sinoatrial node. *FEBS Lett* 481: 73–76, 2000.
8. Boyett MR, Honjo H, Kodama I. The sinoatrial node, a heterogeneous pacemaker structure. *Cardiovasc Res* 47: 658–687, 2000.
9. Chen B, Wu Y, Mohler PJ, Anderson ME, Song LS. Local control of Ca^{2+} -induced Ca^{2+} release in mouse sinoatrial node cells. *J Mol Cell Cardiol* 47: 706–715, 2009.
10. Cho HS, Takano M, Noma A. The electrophysiological properties of spontaneously beating pacemaker cells isolated from mouse sinoatrial node. *J Physiol* 550: 169–180, 2003.
11. Clark RB, Mangoni ME, Lueger A, Couette B, Nargeot J, Giles WR. A rapidly activating delayed rectifier K^+ current regulates pacemaker activity in adult mouse sinoatrial node cells. *Am J Physiol Heart Circ Physiol* 286: H1757–H1766, 2004.
12. Demion M, Bois P, Launay P, Guinamard R. TRPM4, a Ca^{2+} -activated nonselective cation channel in mouse sino-atrial node cells. *Cardiovasc Res* 73: 531–538, 2007.
13. Demir SS, Clark JW, Murphey CR, Giles WR. A mathematical model of a rabbit sinoatrial node cell. *Am J Physiol Cell Physiol* 266: C832–C852, 1994.
14. Denyer JC, Brown HF. Rabbit sino-atrial node cells: isolation and electrophysiological properties. *J Physiol* 428: 405–424, 1990.
15. Despa S, Bossuyt J, Han F, Ginsburg KS, Jia LG, Kutchai H, Tucker AL, Bers DM. Phospholemman-phosphorylation mediates the beta-adrenergic effects on Na^+/K^+ pump function in cardiac myocytes. *Circ Res* 97: 252–259, 2005.
16. Dokos S, Celler B, Lovell N. Ion currents underlying sinoatrial node pacemaker activity: a new single cell mathematical model. *J Theor Biol* 181: 245–272, 1996.
17. Faber GM, Rudy Y. Calsequestrin mutation and catecholaminergic polymorphic ventricular tachycardia: a simulation study of cellular mechanism. *Cardiovasc Res* 75: 79–88, 2007.

18. Fukuzaki K, Sato T, Miki T, Seino S, Nakaya H. Role of sarcolemmal ATP-sensitive K^+ channels in the regulation of sinoatrial node automaticity: an evaluation using Kir6.2-deficient mice. *J Physiol* 586: 2767–2778, 2008.
19. Greenstein JL, Tanskanen AJ, Winslow RL. Modeling the actions of β -adrenergic signaling on excitation-contraction coupling processes. *Ann NY Acad Sci* 1015: 16–27, 2004.
20. Guo J, Mitsuiye T, Noma A. The sustained inward current in sino-atrial node cells of guinea-pig heart. *Pflügers Arch* 433: 390–396, 1997.
21. Guo J, Ono K, Noma A. A sustained inward current activated at the diastolic potential range in rabbit sino-atrial node cells. *J Physiol* 483: 1–13, 1995.
22. Hagiwara N, Irisawa H, Kameyama M. Contribution of two types of calcium currents to the pacemaker potentials of rabbit sino-atrial node cells. *J Physiol* 395: 233–253, 1988.
23. Han F, Bossuyt J, Despa S, Tucker AL, Bers DM. Phospholemman phosphorylation mediates the protein kinase C-dependent effects on Na^+/K^+ pump function in cardiac myocytes. *Circ Res* 99: 1376–1383, 2006.
24. Heath BM, Terrar DA. The deactivation kinetics of the delayed rectifier components I_{Kr} and I_{Ks} in guinea-pig isolated ventricular myocytes. *Exp Physiol* 81: 605–621, 1996.
25. Herrmann S, Stieber J, Ludwig A. Pathophysiology of HCN channels. *Pflügers Arch* 454: 517–522, 2007.
26. Herrmann S, Stieber J, Stockl G, Hofmann F, Ludwig A. HCN4 provides a “depolarization reserve” and is not required for heart rate acceleration in mice. *EMBO J* 26: 4423–4432, 2007.
27. Himeno Y, Toyoda F, Satoh H, Amano A, Cha CY, Matsuura H, Noma A. Minor contribution of cytosolic Ca^{2+} transients to the pacemaker rhythm in guinea pig sinoatrial node cells. *Am J Physiol Heart Circ Physiol* 300: H251–H261, 2011.
28. Hund TJ, Rudy Y. Rate dependence and regulation of action potential and calcium transient in a canine cardiac ventricular cell model. *Circulation* 110: 3168–3174, 2004.
29. Huser J, Blatter LA, Lipsius SL. Intracellular Ca^{2+} release contributes to automaticity in cat atrial pacemaker cells. *J Physiol* 524: 415–422, 2000.
30. Ju YK, Chu Y, Chalet H, Lai D, Gervasio OL, Graham RM, Cannell MB, Allen DG. Store-operated Ca^{2+} influx and expression of TRPC genes in mouse sinoatrial node. *Circ Res* 100: 1605–1614, 2007.
31. Kharche S, Higham J, Lei M, Zhang H. *Functional Roles of Ionic Currents in a Membrane Delimited Mouse Sino-Atrial Node Cell Model* (online). <http://www.cinc.org/archives/2010/pdf/0421.pdf> [6 July 2011].
32. Kharche S, Lüdtke N, Panzeri S, HZ. A global sensitivity index for biophysically detailed cardiac cell models: a computational approach. *LNCS* 5528: 10, 2009.
33. Kneller J, Ramirez RJ, Chartier D, Courtemanche M, Nattel S. Time-dependent transients in an ionically based mathematical model of the canine atrial action potential. *Am J Physiol Heart Circ Physiol* 282: H1437–H1451, 2002.
34. Kodama I, Nikmaram MR, Boyett MR, Suzuki R, Honjo H, Owen JM. Regional differences in the role of the Ca^{2+} and Na^+ currents in pacemaker activity in the sinoatrial node. *Am J Physiol Heart Circ Physiol* 272: H2793–H2806, 1997.
35. Krogh-Madsen T, Schaffer P, Skriver AD, Taylor LK, Pelzmann B, Koidl B, Guevara MR. An ionic model for rhythmic activity in small clusters of embryonic chick ventricular cells. *Am J Physiol Heart Circ Physiol* 289: H398–H413, 2005.
36. Kurata Y, Hisatome I, Imanishi S, Shibamoto T. Dynamical description of sinoatrial node pacemaking: improved mathematical model for primary pacemaker cell. *Am J Physiol Heart Circ Physiol* 283: H2074–H2101, 2002.
37. Kurata Y, Matsuda H, Hisatome I, Shibamoto T. Regional difference in dynamical property of sinoatrial node pacemaking: role of Na^+ channel current. *Biophys J* 95: 951–977, 2008.
38. Lakatta EG, Vinogradova TM, Maltsev VA. The missing link in the mystery of normal automaticity of cardiac pacemaker cells. *Ann NY Acad Sci* 1123: 41–57, 2008.
39. Lei M, Goddard C, Liu J, Leoni AL, Royer A, Fung SS, Xiao G, Ma A, Zhang H, Charpentier F, Vandenberg JL, Colledge WH, Grace AA, Huang CL. Sinus node dysfunction following targeted disruption of the murine cardiac sodium channel gene *Scn5a*. *J Physiol* 567: 387–400, 2005.
40. Lei M, Honjo H, Kodama I, Boyett MR. Characterisation of the transient outward K^+ current in rabbit sinoatrial node cells. *Cardiovasc Res* 46: 433–441, 2000.
41. Lei M, Jones SA, Liu J, Lancaster MK, Fung SS, Dobrzynski H, Camelliti P, Maier SK, Noble D, Boyett MR. Requirement of neuronal and cardiac-type sodium channels for murine sinoatrial node pacemaking. *J Physiol* 559: 835–848, 2004.
42. Lei M, Zhang H, Grace AA, Huang CL. SCN5A and sinoatrial node pacemaker function. *Cardiovasc Res* 74: 356–365, 2007.
43. Liao Z, Lockhead D, Larson ED, Proenza C. Phosphorylation and modulation of hyperpolarization-activated HCN4 channels by protein kinase A in the mouse sinoatrial node. *J Gen Physiol* 136: 247–258.
44. Lipsius SL, Huser J, Blatter LA. Intracellular Ca^{2+} release sparks atrial pacemaker activity. *News Physiol Sci* 16: 101–106, 2001.
45. Liu J, Dobrzynski H, Yanni J, Boyett MR, Lei M. Organisation of the mouse sinoatrial node: structure and expression of HCN channels. *Cardiovasc Res* 73: 729–738, 2007.
46. Livshitz L, Rudy Y. Uniqueness and stability of action potential models during rest, pacing, and conduction using problem-solving environment. *Biophys J* 97: 1265–1276, 2009.
47. Lomax AE, Rose RA, Giles WR. Electrophysiological evidence for a gradient of G protein-gated K^+ current in adult mouse atria. *Br J Pharmacol* 140: 576–584, 2003.
48. Lyashkov AE, Juhaszova M, Dobrzynski H, Vinogradova TM, Maltsev VA, Juhasz O, Spurgeon HA, Sollott SJ, Lakatta EG. Calcium cycling protein density and functional importance to automaticity of isolated sinoatrial nodal cells are independent of cell size. *Circ Res* 100: 1723–1731, 2007.
49. Maltsev VA, Lakatta EG. Cardiac pacemaker cell failure with preserved I_f , I_{CaL} , and I_{Kr} : a lesson about pacemaker function learned from ischemia-induced bradycardia. *J Mol Cell Cardiol* 42: 289–294, 2007.
50. Maltsev VA, Lakatta EG. Synergism of coupled subsarcolemmal Ca^{2+} clocks and sarcolemmal voltage clocks confers robust and flexible pacemaker function in a novel pacemaker cell model. *Am J Physiol Heart Circ Physiol* 296: H594–H615, 2009.
51. Maltsev VA, Vinogradova TM, Bogdanov KY, Lakatta EG, Stern MD. Diastolic calcium release controls the beating rate of rabbit sinoatrial node cells: numerical modeling of the coupling process. *Biophys J* 86: 2596–2605, 2004.
52. Mangoni ME, Couette B, Bourinet E, Platzer J, Reimer D, Striessnig J, Nargeot J. Functional role of L-type Cav1.3 Ca^{2+} channels in cardiac pacemaker activity. *Proc Natl Acad Sci USA* 100: 5543–5548, 2003.
53. Mangoni ME, Couette B, Marger L, Bourinet E, Striessnig J, Nargeot J. Voltage-dependent calcium channels and cardiac pacemaker activity: from ionic currents to genes. *Prog Biophys Mol Biol* 90: 38–63, 2006.
54. Mangoni ME, Nargeot J. Genesis and regulation of the heart automaticity. *Physiol Rev* 88: 919–982, 2008.
55. Mangoni ME, Nargeot J. Properties of the hyperpolarization-activated current (I_f) in isolated mouse sino-atrial cells. *Cardiovasc Res* 52: 51–64, 2001.
56. Mangoni ME, Traboulsie A, Leoni AL, Couette B, Marger L, Le Quang K, Kupfer E, Cohen-Solal A, Vilar J, Shin HS, Escande D, Charpentier F, Nargeot J, Lory P. Bradycardia and slowing of the atrioventricular conduction in mice lacking Cav3.1/ $\alpha 1G$ T-type calcium channels. *Circ Res* 98: 1422–1430, 2006.
57. Masumiya H, Yamamoto H, Hemberger M, Tanaka H, Shigenobu K, Chen SR, Furukawa T. The mouse sino-atrial node expresses both the type 2 and type 3 Ca^{2+} release channels/ryanodine receptors. *FEBS Lett* 553: 141–144, 2003.
58. Matsuura H, Ehara T, Ding WG, Omatsu-Kanbe M, Isono T. Rapidly and slowly activating components of delayed rectifier K^+ current in guinea-pig sino-atrial node pacemaker cells. *J Physiol* 540: 815–830, 2002.
59. Mills GD, Harris DM, Chen X, Houser SR. Intracellular sodium determines frequency-dependent alterations in contractility in hypertrophied feline ventricular myocytes. *Am J Physiol Heart Circ Physiol* 292: H1129–H1138, 2007.
60. Mitsuiye T, Guo J, Noma A. Nicardipine-sensitive Na^+ -mediated single channel currents in guinea-pig sinoatrial node pacemaker cells. *J Physiol* 521: 69–79, 1999.
61. Moosmang S, Stieber J, Zong X, Biel M, Hofmann F, Ludwig A. Cellular expression and functional characterization of four hyperpolarization-activated pacemaker channels in cardiac and neuronal tissues. *Eur J Biochem* 268: 1646–1652, 2001.

62. Nikmaram MR, Liu J, Abdelrahman M, Dobrzynski H, Boyett MR, Lei M. Characterization of the effects of ryanodine, TTX, E-4031 and 4-AP on the sinoatrial and atrioventricular nodes. *Prog Biophys Mol Biol* 96: 452–464, 2008.
63. Noble D. A modification of the Hodgkin-Huxley equations applicable to Purkinje fibre action and pace-maker potentials. *J Physiol* 160: 317–352, 1962.
64. Ono K, Shibata S, Iijima T. Pacemaker mechanism of porcine sino-atrial node cells. *J Smooth Muscle Res* 39: 195–204, 2003.
65. Oudit GY, Kassiri Z, Sah R, Ramirez RJ, Zobel C, Backx PH. The molecular physiology of the cardiac transient outward potassium current (I_{to}) in normal and diseased myocardium. *J Mol Cell Cardiol* 33: 851–872, 2001.
66. Rose RA, Kabir MG, Backx PH. Altered heart rate and sinoatrial node function in mice lacking the cAMP regulator phosphoinositide 3-kinase- γ . *Circ Res* 101: 1274–1282, 2007.
67. Sarai N, Matsuoka S, Kuratomi S, Ono K, Noma A. Role of individual ionic current systems in the SA node hypothesized by a model study. *Jpn J Physiol* 53: 125–134, 2003.
68. Satoh H. Sino-atrial nodal cells of mammalian hearts: ionic currents and gene expression of pacemaker ionic channels. *J Smooth Muscle Res* 39: 175–193, 2003.
69. Shannon TR, Chu G, Kranias EG, Bers DM. Phospholamban decreases the energetic efficiency of the sarcoplasmic reticulum Ca pump. *J Biol Chem* 276: 7195–7201, 2001.
70. Shannon TR, Ginsburg KS, Bers DM. Quantitative assessment of the SR Ca^{2+} leak-load relationship. *Circ Res* 91: 594–600, 2002.
71. Shannon TR, Ginsburg KS, Bers DM. Reverse mode of the sarcoplasmic reticulum calcium pump and load-dependent cytosolic calcium decline in voltage-clamped cardiac ventricular myocytes. *Biophys J* 78: 322–333, 2000.
72. Shannon TR, Wang F, Bers DM. Regulation of cardiac sarcoplasmic reticulum Ca release by luminal [Ca] and altered gating assessed with a mathematical model. *Biophys J* 89: 4096–4110, 2005.
73. Shannon TR, Wang F, Puglisi J, Weber C, Bers DM. A mathematical treatment of integrated Ca dynamics within the ventricular myocyte. *Biophys J* 87: 3351–3371, 2004.
74. Shinagawa Y, Satoh H, Noma A. The sustained inward current and inward rectifier K^{+} current in pacemaker cells dissociated from rat sinoatrial node. *J Physiol* 523: 593–605, 2000.
75. Sun H, Varela D, Chartier D, Ruben PC, Nattel S, Zamponi GW, Leblanc N. Differential interactions of Na^{+} channel toxins with T-type Ca^{2+} channels. *J Gen Physiol* 132: 101–113, 2008.
76. Tao T, O'Neill SC, Diaz ME, Li YT, Eisner DA, Zhang H. Alternans of cardiac calcium cycling in a cluster of ryanodine receptors: a simulation study. *Am J Physiol Heart Circ Physiol* 295: H598–H609, 2008.
77. Varghese A, Sell GR. A conservation principle and its effect on the formulation of Na-Ca exchanger current in cardiac cells. *J Theor Biol* 189: 33–40, 1997.
78. Veldkamp MW, Wilders R, Baartscheer A, Zegers JG, Bezzina CR, Wilde AA. Contribution of sodium channel mutations to bradycardia and sinus node dysfunction in LQT3 families. *Circ Res* 92: 976–983, 2003.
79. Verheijck EE, van Ginneken AC, Bourrier J, Bouman LN. Effects of delayed rectifier current blockade by E-4031 on impulse generation in single sinoatrial nodal myocytes of the rabbit. *Circ Res* 76: 607–615, 1995.
80. Verheijck EE, van Kempen MJ, Veereschild M, Lurvink J, Jongsma HJ, Bouman LN. Electrophysiological features of the mouse sinoatrial node in relation to connexin distribution. *Cardiovasc Res* 52: 40–50, 2001.
81. Verkerk AO, van Borren MM, Peters RJ, Broekhuis E, Lam KY, Coronel R, de Bakker JM, Tan HL, Wilders R. Single cells isolated from human sinoatrial node: action potentials and numerical reconstruction of pacemaker current. *Conf Proc IEEE Eng Med Biol Soc* 2007: 904–907, 2007.
82. Vinogradova TM, Sirenko S, Lyashkov AE, Younes A, Li Y, Zhu W, Yang D, Ruknudin AM, Spurgeon H, Lakatta EG. Constitutive phosphodiesterase activity restricts spontaneous beating rate of cardiac pacemaker cells by suppressing local Ca^{2+} releases. *Circ Res* 102: 761–769, 2008.
83. Wilders R. Computer modelling of the sinoatrial node. *Med Biol Eng Comput* 45: 189–207, 2007.
84. Wu Y, Gao Z, Chen B, Koval OM, Singh MV, Guan X, Hund TJ, Kutschke W, Sarma S, Grumbach IM, Wehrens XH, Mohler PJ, Song LS, Anderson ME. Calmodulin kinase II is required for fight or flight sinoatrial node physiology. *Proc Natl Acad Sci USA* 106: 5972–5977, 2009.
85. Xu H, Guo W, Nerbonne JM. Four kinetically distinct depolarization-activated K^{+} currents in adult mouse ventricular myocytes. *J Gen Physiol* 113: 661–678, 1999.
86. Xu H, Li H, Nerbonne JM. Elimination of the transient outward current and action potential prolongation in mouse atrial myocytes expressing a dominant negative $Kv4 \alpha$ subunit. *J Physiol* 519: 11–21, 1999.
87. Yin J, Wang Y, Li Q, Shang Z, Su S, Cheng Y, Xu Y. Effects of nanomolar concentration dihydropyridine on calcium current and intracellular calcium in guinea pig ventricular myocytes. *Life Sci* 76: 613–628, 2004.
88. Zhang H, Holden AV, Boyett MR. Sustained inward current and pacemaker activity of mammalian sinoatrial node. *J Cardiovasc Electrophysiol* 13: 809–812, 2002.
89. Zhang H, Holden AV, Kodama I, Honjo H, Lei M, Varghese T, Boyett MR. Mathematical models of action potentials in the periphery and center of the rabbit sinoatrial node. *Am J Physiol Heart Circ Physiol* 279: H397–H421, 2000.
90. Zhang H, Zhao Y, Lei M, Dobrzynski H, Liu JH, Holden AV, Boyett MR. Computational evaluation of the roles of Na^{+} current, i_{NaP} , and cell death in cardiac pacemaking and driving. *Am J Physiol Heart Circ Physiol* 292: H165–H174, 2007.
91. Zhang Z, Xu Y, Song H, Rodriguez J, Tuteja D, Namkung Y, Shin HS, Chiamvimonvat N. Functional roles of $Ca_v1.3$ (α_{1D}) calcium channel in sinoatrial nodes: insight gained using gene-targeted null mutant mice. *Circ Res* 90: 981–987, 2002.
92. Zhou Z, Lipsius SL. T-type calcium current in latent pacemaker cells isolated from cat right atrium. *J Mol Cell Cardiol* 26: 1211–1219, 1994.